Forecasting Quasi-Linear Convective System Tornado Potential Using the Warn-on-Forecast System (WoFS)

KELSEY C. BRITT,[a,b] PATRICK S. SKINNER,[a,b,c] MATTHEW C. BROWN,[b] PAMELA L. HEINSELMAN,[b,c] AND ADAM J. CLARK[b,c]

[a] *Cooperative Institute for Severe and High-Impact Weather Research and Operations, University of Oklahoma, Norman, Oklahoma*
[b] *NOAA/OAR National Severe Storms Laboratory, Norman, Oklahoma*
[c] *School of Meteorology, University of Oklahoma, Norman, Oklahoma*

(Manuscript received 7 May 2025, in final form 17 December 2025, accepted 12 January 2026)

ABSTRACT: Accurately forecasting mesovortex tornado potential within quasi-linear convective systems (QLCSs) remains a major challenge. One technique used to support QLCS tornado warning operations is the three ingredients method (3IM), which is based on system balance modulated by line-normal vertical wind shear. However, observational studies examining prolific mesovortex- and tornado-producing QLCSs have identified a substantial line-parallel component of the low-level environmental shear field, which is unaccounted for in the 3IM. Recent numerical studies suggest that line-parallel shear promotes the development of strong, cyclonic mesovortices, thereby increasing the overall likelihood of QLCS tornadoes. Motivated by these recent findings, this proof-of-concept study represents the first attempt to quantify the physical factors comprising the 3IM using a prototype composite forecast parameter QTor. QTor integrates near-storm environmental vertical wind shear components with leading-line geometry to generate system-relative probabilistic forecasts for mesovortex tornado potential. QTor is evaluated using three tornadic QLCS cases and one null case within the Warn-on-Forecast System (WoFS), leveraging object-based methods to identify QLCS structures and isolate their leading lines. Results indicate that QTor forecasts show promise in effectively identifying areas conducive to mesovortex tornado development, providing qualitatively accurate probabilistic forecasts of tornadic portions of the QLCSs with up to 3 h of lead time.

SIGNIFICANCE STATEMENT: Squall-line tornadoes are difficult to forecast due to their small size and transient nature, leading to lower predictability and shorter warning lead times compared to supercell tornadoes. This study introduces QTor, a new forecasting parameter designed to predict tornado potential within squall lines. Results indicate that QTor may effectively identify areas of increased tornado likelihood, predicting tornadic portions of a squall line over 3 h in advance. While still in early development, QTor shows great promise and has the potential to enhance squall-line tornado prediction in the future.

KEYWORDS: Severe storms; Tornadoes; Convective storms; Forecasting techniques; Numerical weather prediction/forecasting

1. Introduction

A large portion of past severe convective storm research has focused on understanding and forecasting supercell thunderstorms (Trapp et al. 2005; Markowski and Richardson 2010; Smith et al. 2012; Brotzge et al. 2013), given their ability to produce significant (EF3+) damaging tornadoes (Trapp et al. 2005). However, supercells are not the exclusive producers of tornadoes and other damaging hazards. Quasi-linear convective systems (QLCSs; Trapp et al. 2005) are linearly oriented mesoscale convective systems (MCSs; Houze 2018) that are capable of producing a variety of dangerous and destructive hazards such as straight-line winds, hail, flash flooding, and tornadoes produced from shallow mesovortices (Atkins et al. 2004; Trapp et al. 2005; Smith et al. 2012; Thompson et al. 2012; Brotzge et al. 2013; Ashley et al. 2019). A radar-based QLCS climatology found that QLCSs account for around 21% and 28% of CONUS tornado and severe wind reports, respectively (Ashley et al. 2019). QLCS hazards can occur year-round, including during the cold season (October–February), when severe weather may be less anticipated by the public (Trapp et al. 2005; Smith et al. 2012; Ashley et al. 2019), and are especially dangerous at night or in the early morning when people are asleep and fatality rates tend to be higher (Ashley et al. 2008). Prediction is further complicated by fast storm motion (SM) and occurrence in areas with complex terrain and limited radar coverage, such as the Southeast United States. As a result, QLCS hazards (especially severe wind and tornadoes) tend to be more difficult to warn and have shorter warning lead times compared to supercells, which presents substantial forecasting and operational challenges (Brotzge et al. 2013).

Mesovortices are meso-γ-scale circulations (2–40 km in diameter; Orlanski 1975; Weisman and Trapp 2003) that typically form along the leading line of a QLCS and are the most intense near the surface (1–2 km AGL; Flournoy and Coniglio 2019). Mesovortices are often transient in nature, meaning they can form and decay on the order of 10 min or less (Mahale et al. 2012; Newman and Heinselman 2012). Consequently, anticipating

Corresponding author: Kelsey C. Britt, kelsbritt@ou.edu

DOI: 10.1175/WAF-D-25-0092.1

© 2026 American Meteorological Society. This published article is licensed under the terms of the default AMS reuse license. For information regarding reuse of this content and general copyright information, consult the AMS Copyright Policy (www.ametsoc.org/PUBSReuseLicenses).

Brought to you by NOAA Library | Unauthenticated | Downloaded 09/14/26 03:13 PM UTC

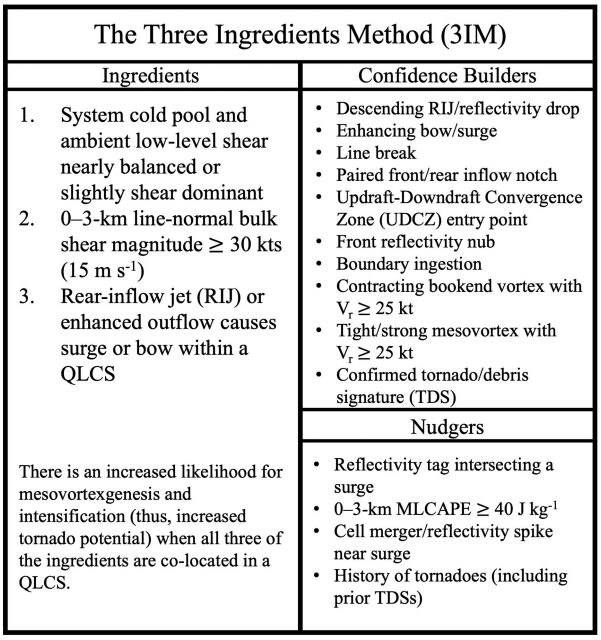


FIG. 1. The main ingredients, confidence builders, and nudgers (i.e., supplemental factors that constitute the 3IM used by NWS forecasters in warning operations for QLCS tornadoes). For more information about 3IM assessment and visualization, refer to the QLCS Reference Sheets at https://www.weather.gov/sgf/qlcs_tornado_training (NWS 2023).

mesovortex tornado potential presents a considerable operational forecasting challenge.

Supercell forecast parameters such as the significant tornado parameter (STP; Thompson et al. 2003, 2012) are used extensively by National Weather Service (NWS) agencies like the Storm Prediction Center (SPC) to assess the tornado potential associated with supercells. However, an equivalent real-time, composite forecast parameter for QLCS tornado likelihood has yet to be developed. The current paradigm for issuing QLCS tornado warnings employed by the NWS is known as the three ingredients method (3IM; Fig. 1; Schaumann and Przybylinksi 2012). The first two ingredients of the 3IM are grounded in Rotunno–Klemp–Weisman (RKW) theory (Rotunno et al. 1988; Weisman and Rotunno 2004), which states that there should be a balance in the circulations associated with the leading edge of the QLCS cold pool and the environmental line-normal wind shear (Fig. 1). This "optimal balanced state" (Rotunno et al. 1988) favors strong and upright low-level updrafts, leading to better vortex–updraft alignment and the enhancement of near-surface rotation (Lee and Wilhelmson 2000).

The fundamental assumption underpinning the 3IM is that system balance should also promote mesovortexgenesis, but this is not always the case, leading to inherent limitations with this technique. First, mesovortices have been observed in environments where the line-normal (LN) shear magnitude is below the 3IM threshold of 15 m s^{-1} (Ungar and Coniglio 2023). Additionally, observational studies examining prolific mesovortex- and tornado-producing QLCSs often note a line-parallel (LP) component in the low-level (≤1 km AGL) shear profile (Funk et al. 1999; Lyza et al. 2017; Flournoy and Coniglio 2019). A recent numerical study by Brown et al. (2024) found that increased LP shear favors stronger, larger, and more persistent mesovortices (particularly cyclonic mesovortices), which is consistent with observational analyses by Ungar and Coniglio (2023), who showed that most instances of cyclonic mesovortex formation occur with at least moderate (≥5 m s^{-1}) low-level LP shear. Additional studies found that tornadic mesovortices tended to be stronger, larger, and more persistent than nontornadic mesovortices (Atkins et al. 2004; Davis and Parker 2014; Pardun et al. 2025). Thus, an environment with more LP shear may also increase the likelihood for mesovortex tornadoes, suggesting that the 3IM is limited by its exclusive focus on LN shear.

Additional weaknesses of the 3IM are driven by its subjective nature and manual application, making it extremely difficult to implement into numerical weather prediction (NWP) guidance and thus limiting its applicability to very short lead times. Its efficacy is also constrained by reliance on low-level radar coverage since the majority of the 3IM ingredients and confidence builders (Fig. 1) require high-fidelity radar reflectivities and radial velocities. Past research has found that meteorologists issuing short-term forecasts for rapidly evolving convective events can experience cognitive overload when condensing large amounts of data into public forecasts (Wilson et al. 2017; Karstens et al. 2018; James et al. 2020). Thus, the 3IM can potentially increase workload and become a time-consuming process for operational meteorologists owing to the inclusion of 10 confidence builders and four "nudgers" aimed at bolstering a forecaster's confidence in issuing a tornado warning for a QLCS (Fig. 1). This can be particularly true during instances of nocturnal or mixed-mode convective events, during which forecasters may be simultaneously tracking numerous storms and/or circulations with varying hazards. Since mesovortex tornadoes can develop and strengthen rapidly, a forecast tool that highlights the areas of increased mesovortex tornado potential without requiring the detailed steps of the 3IM may help reduce the cognitive demand on forecasters (Wilson et al. 2017).

The proliferation of convection-allowing NWP models facilitates the transformation of the 3IM into an objective framework, creating a simpler and more effective approach for predicting QLCS mesovortex tornadoes. This study serves as a proof of concept introducing a new composite forecast parameter for assessing QLCS mesovortex tornado potential. Given the exploratory nature of this study and the limited number and diversity of case studies examined, the results are not intended for quantitative verification or operational application at this stage. Instead, the parameter is presented as an initial framework that will require further refinement, testing, and evaluation across a broader range of QLCS events before operational consideration. This new parameter is implemented into the Warn-on-Forecast System (WoFS; Stensrud et al. 2009, 2013; Wheatley et al. 2015; Jones et al. 2016; Heinselman et al. 2024; Martin et al. 2024) to provide probabilistic forecasts for QLCS tornado potential for four case studies. WoFS is a rapidly updating, movable

Brought to you by NOAA Library | Unauthenticated | Downloaded 09/14/26 03:13 PM UTC

domain, convection-allowing ensemble developed by the National Severe Storms Laboratory designed to improve forecasts for hazardous weather and is in the first steps of transitioning to operations at the NWS. WoFS provides skillful forecasts for a wide variety of severe convective events, including tornadic thunderstorms (Yussouf et al. 2013; Wheatley et al. 2015; Yussouf et al. 2015; Jones et al. 2016; Skinner et al. 2018; Flora et al. 2019; Britt et al. 2020; Galarneau et al. 2022), flash flooding events (Yussouf et al. 2016; Lawson et al. 2018; Yussouf and Knopfmeier 2019; Yussouf et al. 2020b), tropical cyclones (Jones et al. 2019; Yussouf et al. 2020a), and QLCSs (Kerr and Alsheimer 2022; Britt et al. 2024).

The composite forecast parameter, called QTor, can be used in tandem with operational radar data and convection-allowing models to provide probabilistic forecasting guidance prior to a potentially tornadic event. QTor leverages new insights into QLCS dynamics, such as the importance of low-level LP shear for fostering intense and long-lived cyclonic mesovortices (Ungar and Coniglio 2023; Brown et al. 2024), whether through the release of horizontal shearing instability (e.g., Lee and Wilhelmson 1997), tilting of horizontal vorticity (Flournoy and Coniglio 2019), or modulations to inflow vorticity attributes (Brown et al. 2026). Thus, LP and LN shear can be incorporated into QTor and used to forecast the potential for mesovortex tornadoes, as tornadic mesovortices are typically stronger and wider than nontornadic mesovortices (Atkins et al. 2004; Marion and Trapp 2021).

The purpose of QTor is twofold. First, it aims to update the 3IM within the context of recent advances in QLCS science toward improved prediction. Second, it transitions the 3IM from a subjective framework to an objective, system-relative framework that incorporates the evolution of the QLCS and its leading-line geometry, rather than relying only on the upstream environment. While designed to be objective, the current implementation uses subjectively assessed SM; future versions will rely entirely on objective SM estimates. Accurately calculating LP and LN shear requires an estimate of line orientation, which can vary along a QLCS's leading edge. Using a single, system-wide orientation results in QTor values that are only valid for portions of the line matching that orientation. To address this, the system-relative method determines the leading-line orientation locally and calculates LP and LN shear relative to that orientation. By adapting to local variations in line orientation, this approach yields QTor values that better represent the spatial variability of the QLCS.

2. Data and methods

QLCSs can develop in a wide range of environments. Therefore, it is important to test QTor's forecast capability and effectiveness over a broad spectrum of cases. QTor is evaluated using three tornadic QLCS case studies that differ in location, season, and mesoscale environment: 15 December 2021, 30 March 2022, and 12 May 2022, as well as a null case on 19 May 2024 (Fig. 2). The 15 December 2021 case was a cold-season derecho that developed in a high-shear environment and produced 101 tornadoes.[1] The 30 March 2022 QLCS developed in a high-shear, low–convective available potential energy (CAPE) (HSLC) environment in the Southeast United States that produced 47 tornadoes. The 12 May 2022 case was a warm-season derecho in a high-CAPE environment that produced 31 tornadoes. Unlike the other cases, the 19 May 2024 QLCS produced three weak tornadoes following a 2-h nontornadic period and is included as a null case.

a. *WoFS*

WoFS[2] is a 36-member ensemble data assimilation (DA) and prediction system designed to provide probabilistic guidance for severe convective events at temporal and spatial scales typical of convective watches and warnings. It is initialized using the High-Resolution Rapid Refresh (HRRR) Data Assimilation System (HRRRDAS; Dowell et al. 2022), with lateral boundary conditions provided by the 1200 UTC operational HRRR forecast, which are perturbed using the first 36 members of the Global Ensemble Prediction System (GEFS; Zhou et al. 2022). The location of the 900 km × 900 km domain varies daily but is typically positioned over the region expected to be the most favorable for severe convection, guided by the SPC's day 1 convective outlook. WoFS members have a 3-km horizontal grid spacing, 51 vertical levels, and are cycled every 15 min using an ensemble Kalman filter (EnKF; Houtekamer and Zhang 2016) from the community Gridpoint Statistical Interpolation analysis system (GSI; Kleist et al. 2009; Hu et al. 2016) DA system. WoFS assimilates Multi-Radar Multi-Sensor (MRMS; Smith et al. 2016) reflectivity, Weather Surveillance Radar-1988 Doppler (WSR-88D) radial velocity, Geostationary Operational Environmental Satellite (GOES) cloud water path retrievals (Jones et al. 2015, 2016, 2020), GOES clear-sky radiances (Jones et al. 2018), and any available conventional observations from a variety of observing systems (e.g., Automated Surface Observing System).

Each WoFS ensemble member employs the NSSL two-moment microphysics scheme (Mansell et al. 2010) and the Rapid Update Cycle (RUC) land surface model (Smirnova et al. 2016). To account for uncertainties in model physics, planetary boundary layer (PBL) and radiation parameterizations vary across ensemble members (see Table 1 in Skinner et al. 2018). PBL schemes include the Yonsei University (YSU; Hong et al. 2006), Mellor–Yamada–Janjić (MYJ; Mellor and Yamada 1982), and the Mellor–Yamada–Nakanishi–Niino (MYNN; Nakanishi and Niino 2004). Half of the ensemble members use the Dudhia shortwave and Rapid Radiative Transfer Model (RRTM) longwave scheme (Dudhia 1989), while the others use the RRTM for global climate models (RRTMG) longwave and shortwave scheme (Iacono et al. 2008). WoFS issues 18-member forecasts that are initialized at the top of the hour and the bottom of the hour, extending to 6- and 3-h lead times, respectively.

[1] Tornado counts are valid for our WoFS domain and the time periods analyzed (Fig. 2).

[2] For the purposes of this study, only the WoFS configuration during the 2021–24 case study period is provided. For a full history of WoFS configuration changes, refer to Heinselman et al. (2024).

Brought to you by NOAA Library | Unauthenticated | Downloaded 09/14/26 03:13 PM UTC

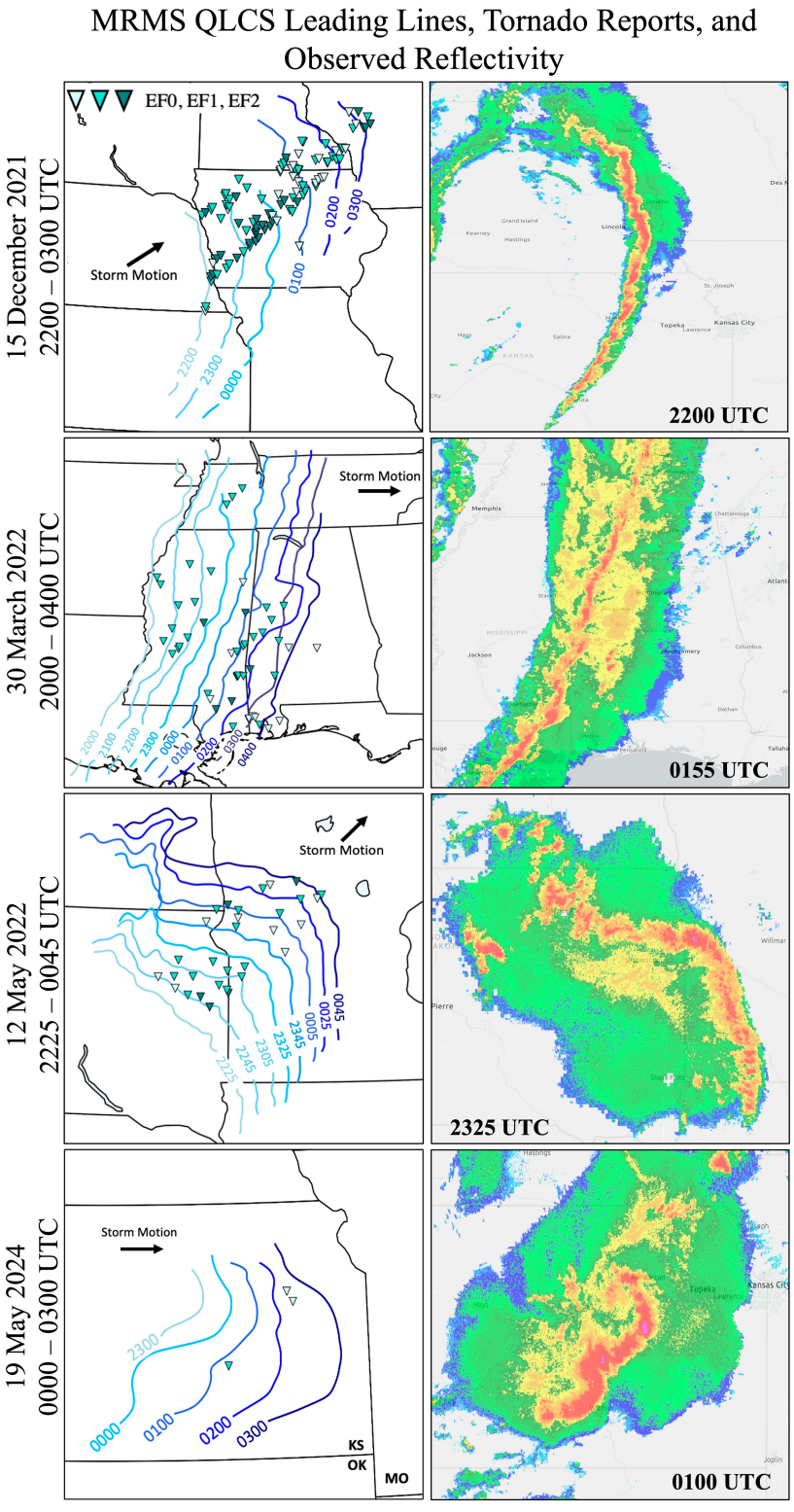


FIG. 2. Overview of the (first row) 15 December 2021, (second row) 30 March 2022, (third row) 12 May 2022, and (fourth row) 19 May 2024 QLCS case studies showing the MRMS leading line with time, tornado reports, and the observed reflectivity from a representative time. Tornado icons represent the starting point for each tornado and are color coded to represent the finalized EF-scale rating. Observed reflectivity is from the National Centers for Environmental Information (NCEI) radar mosaic.

Brought to you by NOAA Library | Unauthenticated | Downloaded 09/14/26 03:13 PM UTC

TABLE 1. Object identification and QLCS classification thresholds for the three case studies. The same reflectivity thresholds are used for MRMS and for the WoFS analysis (or 0-min forecast), but these thresholds change for all subsequent WoFS forecast times (5–360 min, in 5-min increments).

Case	Min reflectivity (dBZ)	Max reflectivity (dBZ)	Min area (grid cells)	Merge distance (grid cells)
15 Dec 2021 MRMS and WoFS analysis	39	44	25	2
30 Mar 2022 MRMS and WoFS analysis	40	45	45	2
12 May 2022 MRMS and WoFS analysis	40	45	6	4
19 May 2024 MRMS and WoFS analysis	40	45	45	2
15 Dec 2021 WoFS forecast	44	49	25	2
30 Mar 2022 WoFS forecast	47	52	45	2
12 May 2022 WoFS forecast	45	50	6	4
19 May 2024 WoFS forecast	47	52	45	2

b. *MRMS*

MRMS generates real-time composite reflectivity from WSR-88D observations collected across the CONUS. These observations are interpolated to the 3-km WoFS grid using a Cressman filter with a 3-km radius of influence (Skinner et al. 2018). Using the Cressman filter results in a smoother reflectivity field compared to using the conservative remapping scheme (Hill et al. 2004), which is advantageous in this study as it results in more contiguous QLCS objects. The resulting gridded composite reflectivity data from MRMS are used to qualitatively assess errors in WoFS QLCS leading-line predictions. Additionally, MRMS is coupled with the WoFS near-storm environment to provide a reference QTor forecast, which is then used for comparison with the WoFS QTor forecasts.

c. *QLCS object identification and isolation*

The object identification and classification for the four QLCS case studies applies the same methods as in Britt et al. (2024) using the automated algorithm from Potvin et al. (2022). The small number of case studies allows for the object identification thresholds to be tuned individually for each event (Table 1). In the future, separate tuning thresholds will not be feasible for a real-time algorithm, but they are used here to demonstrate the optimal performance of QTor for these specific cases.

Two separate minimum and maximum reflectivity thresholds are used for the WoFS forecasts (Table 1). The first threshold represents the analysis (i.e., the 0-min forecast), while the second threshold is for all subsequent forecast times in 5-min increments (5–360 min; Table 1). The minimum and maximum reflectivity threshold for the analysis is the same as those used for MRMS, as DA will more closely fit MRMS observations in the analysis. However, the reflectivity for the WoFS forecasts is driven primarily by the microphysics scheme, which tends to have a high bias relative to MRMS (Britt et al. 2024).

After identifying all possible QLCS objects in WoFS and MRMS, the next step is to isolate the QLCS of interest for each case study, referred to as the object isolation process. This process is a semimanual, subjective process where only the QLCS object(s) associated with the case study are retained, while other objects are removed. This is also the last step in which multiple objects belonging to the same QLCS can be merged together. The isolation process results in only one object per MRMS 5-min output or per WoFS ensemble member for every 5-min output. The subjective nature of the object isolation process is specific to this proof-of-concept study, ensuring that the identified QLCS object(s) are consistent with the case study being evaluated. Future implementations of the QTor algorithm will not require this step, as QTor will be computed for each QLCS object across the domain in real-time operations.

d. *QLCS leading-line identification*

After isolating the QLCS object, the next step is to identify and extract its leading line. Determining which side of the QLCS object contains the leading line uses a general SM vector that is manually estimated using radar reflectivity (see section 4 for more information about how the SM calculation will be automated in future work). For example, the SM of the 30 March 2022 QLCS is to the east (Fig. 2) so the leading line will be located along the eastern edge of the QLCS object. The SM is decomposed into its zonal (longitudinal) and meridional (latitudinal) components. If the components are positive, then the search is done along the QLCS object's leading edge zonally for the easternmost points (Fig. 3a) and meridionally for the northernmost points (Fig. 3b). Figure 3 shows this process demonstrated for a QLCS moving to the east (Fig. 3a) and moving to the north (Fig. 3b). In contrast, if the components are negative, the search is conducted along the QLCS zonally for the westernmost points and meridionally for the southernmost points.

The zonal and meridional points are stored in separate lists and undergo quality control (QC) to remove erroneous points. If the SM is purely zonal or meridional, only the relevant list is retained for QC. QC consists of first identifying the QLCS object's centerline (see Britt et al. 2024 for more details), which is the line that runs down the center of the QLCS object. The centerline serves as a reference line for filtering the points that are not on the leading line. A KDTree nearest-neighbor approach (Pedregosa et al. 2011) determines the closest centerline point to each of the leading-line points. Using this reference, a vector is created between the

Brought to you by NOAA Library | Unauthenticated | Downloaded 09/14/26 03:13 PM UTC

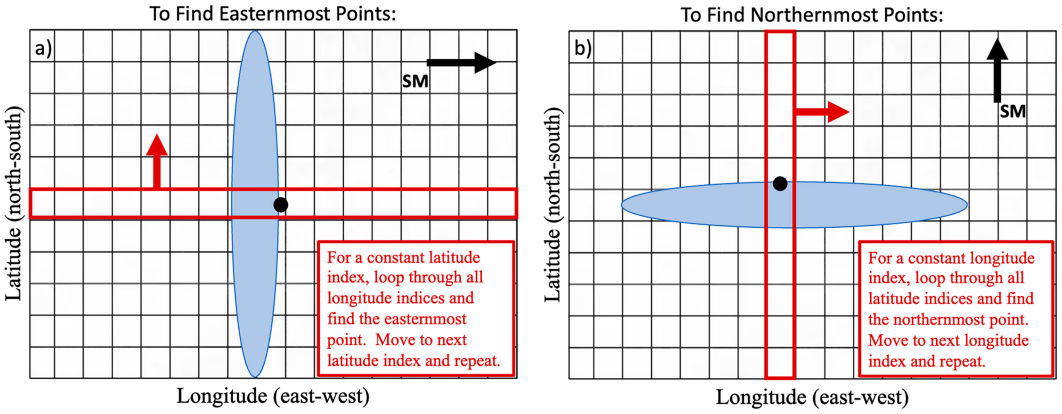


FIG. 3. Simplified example showing the process of finding the (a) easternmost leading line points given a QLCS (blue ellipse) with an easterly SM (black arrow) and (b) northernmost leading line points given a QLCS with a northerly SM. The red rectangle represents the indices/grid boxes that are being looped through, the red arrows illustrate the direction that the box will move when the process is repeated, and the black dot denotes the (a) easternmost or (b) northernmost point that is identified.

centerline and leading-line points. Any points misaligned with the expected SM are excluded (i.e., not in the same geometric quadrant).

After QC is completed, the zonal and meridional lists are merged and resorted to create a continuous leading line. A KDTree nearest-neighbor approach orders the points by defining the start and end points of the leading line and iteratively selecting the nearest unsorted point. This sorting method progresses from the northwest corner to the southeast corner of the WoFS domain. In cases like the 30 March 2022 case, where the QLCS is oriented north–south, the sorting follows the north-to-south order. Finally, the leading line is smoothed using a 2D Gaussian filter with a two-gridpoint radius.

1) LEADING-LINE SHEAR ANALYSIS

LN and LP shear depend on the orientation of the leading line, so the local orientation is determined at each point to calculate the line-relative values. This is done by iterating through all leading-line points and selecting the 10 nearest points on each side of the point of interest. Although the leading-line points are not necessarily equally spaced, on average they are spaced 3 km apart, which typically results in a segment length of 60 km. Of those nearest points, only the endpoints are used to calculate the local orientation, which in this study is defined as degrees counterclockwise from east (0°).

The next step is to define the upstream sector of the QLCS for extracting the WoFS shear data (Fig. 4). To the authors' knowledge, no prior studies have defined a distance ahead of a QLCS representing the near-inflow environment. However, studies on supercell inflow environments suggest defining the near-field environment as the first 0–40 km from the storm (Parker 2014; Coffer et al. 2017; Flournoy et al. 2020; Britt et al. 2020). Assuming a similar distance for QLCSs, we project the leading line forward 40 km and normal to each point's local orientation. In other words, for each leading-line point, we calculate a point that is 40 km ahead and perpendicular to the local orientation at that point. Repeating this process for each leading-line point will form a projection line (i.e., the leading line that is projected forward by 40 km; Fig. 4a). The equations to calculate each of the projection line points are as follows:

$$\theta_{\perp} = \theta_{\text{local}} \pm 90°, \tag{1}$$

$$x_{\text{proj}} = x_{\text{LL}} + [\text{dist} \times \cos(\theta_{\perp})], \tag{2}$$

$$y_{\text{proj}} = y_{\text{LL}} + [\text{dist} \times \sin(\theta_{\perp})], \tag{3}$$

where $\theta_{\perp}$ is the angle normal to the local orientation of the leading-line point (θ_{local}), x_{proj} and y_{proj} are the x and y components of the projection line point, x_{LL} and y_{LL} are the x and y components of the leading-line point, and dist is 40 km. Note that in Eq. (1), the angle normal to the local orientation is calculated either by adding or subtracting 90° depending on SM.

The projection line (Fig. 4a) must also go through a QC process to ensure it is ahead of the leading line. A QC polygon is created that consists of the leading line and two additional lines extending the leading line's endpoints to the corner of the WoFS domain trailing the SM (Fig. 4b). This conical polygon encloses the space behind the leading line (Fig. 4b). The Shapely Python package is used to verify whether or not each projection line point is contained within the QC polygon. If the point is in the polygon, its x and y components are recalculated using the complement angle to $\theta_{\perp}$. In other words, we test points in both directions orthogonal to the leading line but only retain points that are not within the QC polygon. This process is repeated for each projection point to ensure each point is outside the QC polygon (i.e., must be ahead of the leading line).

Once identified, a zero-width Shapely buffer using a Minkowski sum technique (Gillies et al. 2023) is added to the projection line to smooth out any irregularities, such as kinks, holes, or

Brought to you by NOAA Library | Unauthenticated | Downloaded 09/14/26 03:13 PM UTC

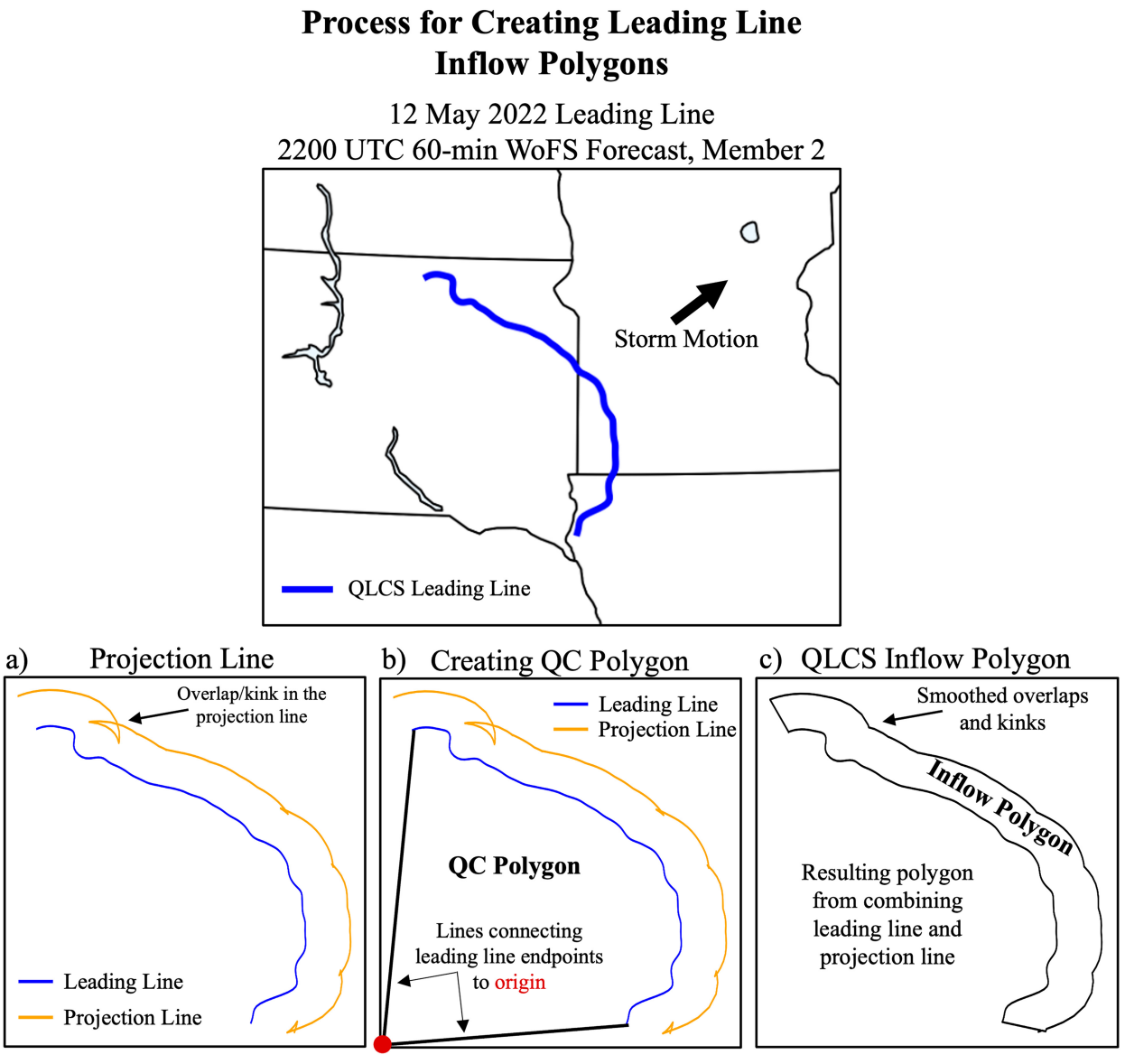


FIG. 4. Leading-line inflow sector development for the 12 May 2022 leading line from the 2200 UTC 60-min WoFS forecast for ensemble member 2. First, (a) the projection line is created by projecting the leading line ahead by 40 km and perpendicular to each point; (b) the QC polygon is created by connecting the endpoints of the leading line back to the domain origin and is used to ensure each point along the projection line is ahead of the leading line; and (c) the leading line and projection line are combined to form the inflow polygon.

overlaps (Fig. 4c). Next, the projection line and leading lines are combined to form a polygon (Fig. 4c). The resulting polygon represents the QLCS inflow environment, in which the WoFS vertical wind shear information will be extracted.

To extract the shear information relative to the QLCS leading line, each WoFS grid box contained within the inflow polygon is matched to the closest leading-line point using a KDTree nearest-neighbor technique. This enables the calculation of LP and LN shear relative to the local orientation angle at each leading-line point (Fig. 5). Following the aforementioned literature, LP shear is calculated over the 0–1-km layer, and LN shear is over the 0–3-km layer (hereafter referred to as LP01 and LN03, respectively).

LP01 shear is calculated by taking the dot product of the local orientation vector and the 0–1-km shear vector that is normalized by the total 0–1-km shear magnitude. The result is multiplied by 100% to yield the percentage of LP01 shear and then multiplied by total 0–1-km shear magnitude to determine the magnitude of LP01 shear. LN03 is calculated similarly, using the dot product between the local orientation vector and the normalized 0–3-km shear vector. This value, also multiplied by 100%, gives the percentage of LP shear within the 0–3-km layer. To determine the magnitude of LN03 shear, the

Brought to you by NOAA Library | Unauthenticated | Downloaded 09/14/26 03:13 PM UTC

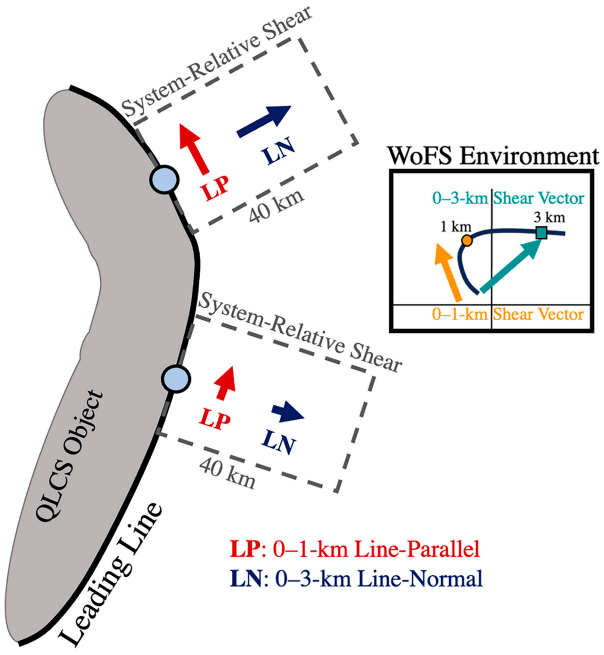


FIG. 5. Schematic illustrating the extraction and calculation of system-relative LP and LN shear components along the QLCS's leading line and how those vectors change with local line orientation.

LP percentage is subtracted from 100% to obtain the LN03 percentage, which is then multiplied by the 0–3-km shear magnitude. The sign (i.e., positive or negative) of the LN03 shear is determined by taking the cross product between the normalized 0–3-km shear vector and the local orientation vector.

The LN03 shear and LP01 shear are calculated for each of the grid boxes contained within the inflow polygon (Fig. 4c) and matched to the nearest point along the leading line. The LP01 shear and LN03 shear for each point along the leading line are calculated as the mean LP01 or LN03 shear from all matched grid boxes.

2) LOCAL TORTUOSITY

Tortuosity is a dimensionless parameter that is used to quantify the curvature of a line (Ciuricä et al. 2019; Britt et al. 2024). For the purposes of this study, local tortuosity is calculated at each point along the QLCS's leading line to assess segment curvature and identify localized bowing structures. The local tortuosity is determined at each leading-line point by considering five points on either side of the point of interest. The shear and tortuosity terms are evaluated on different spatial scales to avoid redundancy between predictors. If calculated on the same scale, shear and tortuosity may become correlated, effectively duplicating information rather than adding independent value to QTor. Therefore, shear terms are evaluated on a more "systemwide" scale, while tortuosity is evaluated on a "segmentwide" scale. The equation for local tortuosity is as follows:

$$\text{Tortuosity}_{\text{local}} = \frac{L_{\text{seg}}}{L_e}, \tag{4}$$

where L_{seg} represents the length of the leading-line segment, obtained by adding the distances between consecutive points within the segment. The L_e denotes endpoint line length, measured as the straight-line distance between the first and last segment points.

e. QLCS mesovortex tornado parameter (QTor)

We incorporate the influence of LN03, LP01, and local tortuosity into a single parameter, QTor. QTor does not explicitly forecast individual mesovortices or tornadoes but identifies portions of the QLCS with the highest potential for mesovortex tornado development. The primary goal of QTor is to transition the subjective, manual 3IM technique into a streamlined parameter that can be automatically generated across a wide range of guidance products, including observations and convection-allowing NWP output. QTor values greater than one indicate areas meeting the base criteria for mesovortex tornado development, with higher values signifying increased favorability. QTor is calculated as follows:

$$\text{QTor} = \frac{\text{LN}_{0\text{–}3}}{10.0\,\text{m s}^{-1}} \times \frac{\text{LP}_{0\text{–}1}}{8.0\,\text{m s}^{-1}} \times T_{\text{factor}}, \tag{5}$$

$$T_{\text{factor}} = \begin{cases} 1, & \text{if Tortuosity}_{\text{local}} \leq 1.05, \\ 2, & \text{if Tortuosity}_{\text{local}} > 1.05, \end{cases} \tag{6}$$

where $\text{LN}_{0\text{–}3}$ represents the magnitude of the LN03 shear and $\text{LP}_{0\text{–}1}$ is the magnitude of the LP01 shear relative to the leading line.

Initially, the LN03 shear threshold was 15.0 m s^{-1} as in the 3IM (Schaumann and Przybylinksi 2012; Gibbs 2021). However, other studies (Ungar and Coniglio 2023) have found that the magnitude of LN shear present in mesovortex-producing environments is often below the 3IM threshold. After performing sensitivity studies (appendix), the LN03 threshold was lowered to 10 m s^{-1}. The LP01 threshold of 8.0 m s^{-1} is motivated by the recent findings of Brown et al. (2024) and additional sensitivity experiments (appendix).

Both the LN03 and LP01 shear terms have a minimum of 0.5 and are capped at 3.0 (appendix). A bottom threshold of 0.5 for each shear term allows QTor to be reduced but not zeroed out if there is no LN03 or LP01 shear as mesovortices may still form in these environments. However, QTor can be zero if LN03 shear is negative, meaning the LN component points behind the leading line. Negative LN03 shear is indicative of an outflow-dominant QLCS segment, where the gust front overruns the main convective line. When this occurs, any mesovortices that develop are quickly shed rearward into the storm, lessening the potential for tornadogenesis. In fact, this follows the first ingredient of the 3IM (Fig. 1; Schaumann and Przybylinksi 2012), where outflow-dominant portions of the QLCS are considered out of balance (according to RKW theory; Rotunno et al. 1988) and, thus, have a lower potential

Brought to you by NOAA Library | Unauthenticated | Downloaded 09/14/26 03:13 PM UTC

for tornadoes. Incorporating the sign of the LN03 shear into the QTor equation is a way to objectively analyze the first ingredient of the 3IM and reduce areas of QTor false alarms.[3]

The final term, local tortuosity, quantifies the curvature along the leading line and identifies local surges or bows along the leading line, which is the third ingredient of the 3IM (Fig. 1; Schaumann and Przybylinksi 2012). Traditionally, forecasters must subjectively analyze the QLCS's leading line for these bowing structures that indicate a higher potential for mesovortex tornadoes. However, incorporating local tortuosity into QTor provides an automated proxy for identification of bowing segments. The tortuosity term is conditional, such that if the local tortuosity is greater than 1.05 (approximately the 75th–90th percentile depending on the case study), then the T_{factor} is set to 2. Conversely, if the tortuosity term is below 1.05, then the T_{factor} is set to one and has no effect on the QTor score. Four methods for treating the tortuosity term were evaluated (appendix), with the conditional approach subjectively performing the best.

f. QTor probabilistic forecasts

Probabilistic guidance products for storm-scale phenomenon are typically not calculated at the gridscale, as small displacement errors may reduce forecast usefulness (Schwartz and Sobash 2017; Roberts et al. 2019). Therefore, neighborhood approaches that spread and smooth the ensemble forecasts are employed to account for spatial uncertainty in shear and local tortuosity. QTor is first calculated using the raw, unsmoothed parameter fields and then smoothed with the neighborhood technique. The neighborhood maximum ensemble probability (Schwartz and Sobash 2017) is used where each grid box is surrounded by a square neighborhood with a radius of 13.5 km (27-km diameter), and its value is replaced by the maximum value within that neighborhood. The resulting field is then smoothed using a convolution kernel filter with a radius of four grid boxes.

QTor is best suited for 0–3- and 0–6-h forecasts to highlight segments of the QLCS's leading line that are most favorable for mesovortex tornado development. Current real-time WoFS guidance employs neighborhood diameters of 9, 15, and 27 km to provide hazard probabilities of individual thunderstorms across areas comparable to typical NWS warnings (Skinner et al. 2023). For this study, the 27-km neighborhood is selected, as the smaller neighborhoods did not adequately visualize the shear, tortuosity, and QTor data.

There are two types of probabilistic products that WoFS uses to represent the severity and likelihood of a forecasted event: percentile and ensemble probability of exceedance products (Wilson et al. 2019; Skinner et al. 2023). The percentile products represent forecasted event severity. The 90th and maximum percentiles are shown in the WoFS online viewer, with the maximum percentile depicting the most extreme outcome. For the purposes of this study, the 75th percentile of QTor is utilized as it provides a "middle ground" between the 50th and 90th percentiles in describing parameter severity. The 75th percentile of the ensemble is computed after applying the neighborhood and smoothing processes. Additionally, neighborhood probability of exceedance is used to quantify the likelihood of QTor meeting a specified threshold. An exceedance threshold of 2.5 was selected because it most effectively highlights areas favorable for mesovortex tornadoes across all three case studies.

WoFS QTor probabilistic forecasts are compared to corresponding forecasts using leading lines associated with MRMS observations. Since MRMS does not contain 0–1- and 0–3-km shear fields like in WoFS, its QTor forecasts will be calculated using the WoFS environment at the start of each forecast, as it best represents the observed environment. The 18-member WoFS forecasts issued at the top and bottom of the hour will be used as representative inflow environments for MRMS QTor calculations, with only the 0–25-min lead times considered to limit spatial displacements with observations. Inflow shear sectors are extracted using the same methods as for WoFS but relative only to the MRMS leading line. MRMS QTor probabilistic swaths are then generated using the same approach as for WoFS. To avoid convective contamination, the MRMS leading line is overlaid on WoFS temperature and moisture fields to ensure it remains approximately aligned with the leading edge of the cold pool in the WoFS environment (not shown).

g. Tornado reports

Tornado reports serve as a verification source for the WoFS QTor forecasts. For each case study, the tornado reports are obtained from the NOAA/NWS Damage Assessment Toolkit (DAT; NOAA 2024). The start and end points for each tornado are collected from the SPC's tornado database (SPC 2023). Given that many of the tornado tracks are relatively short, only the starting point of each tornado is plotted for all figures. In cases where supercell tornadoes also occurred (e.g., 30 March 2022), these tornadoes were manually excluded to retain only those associated with the QLCS. There are inherent limitations in using tornado reports, including the potential for missed tornadoes in unpopulated areas and the misclassification of weak QLCS tornadoes as straight-line winds (Trapp et al. 2005; Skow and Cogil 2017), or vice versa (Thompson 2023).

3. Results

a. 15 December 2021 Iowa derecho

The 15 December 2021 QLCS developed along a dryline in west-central Kansas around 1800 UTC, tracking northeast through Kansas, Nebraska, Missouri, Minnesota (MN), and Iowa before dissipating in Wisconsin around 0430 UTC 16 December 2021. This event was historic for both Iowa and the United States, producing 63 confirmed tornadoes in Iowa alone, including 21 rated EF2 (Fig. 2). It shattered the state's single-day tornado record (previously 35 on 31 August 2014) and set a new record for the most EF2 tornadoes in a single day, surpassing

[3] Considering the sign of LN03 shear removed a false alarm signature on the southern, nontornadic portion of the 12 May 2022 QLCS.

Brought to you by NOAA Library | Unauthenticated | Downloaded 09/14/26 03:13 PM UTC

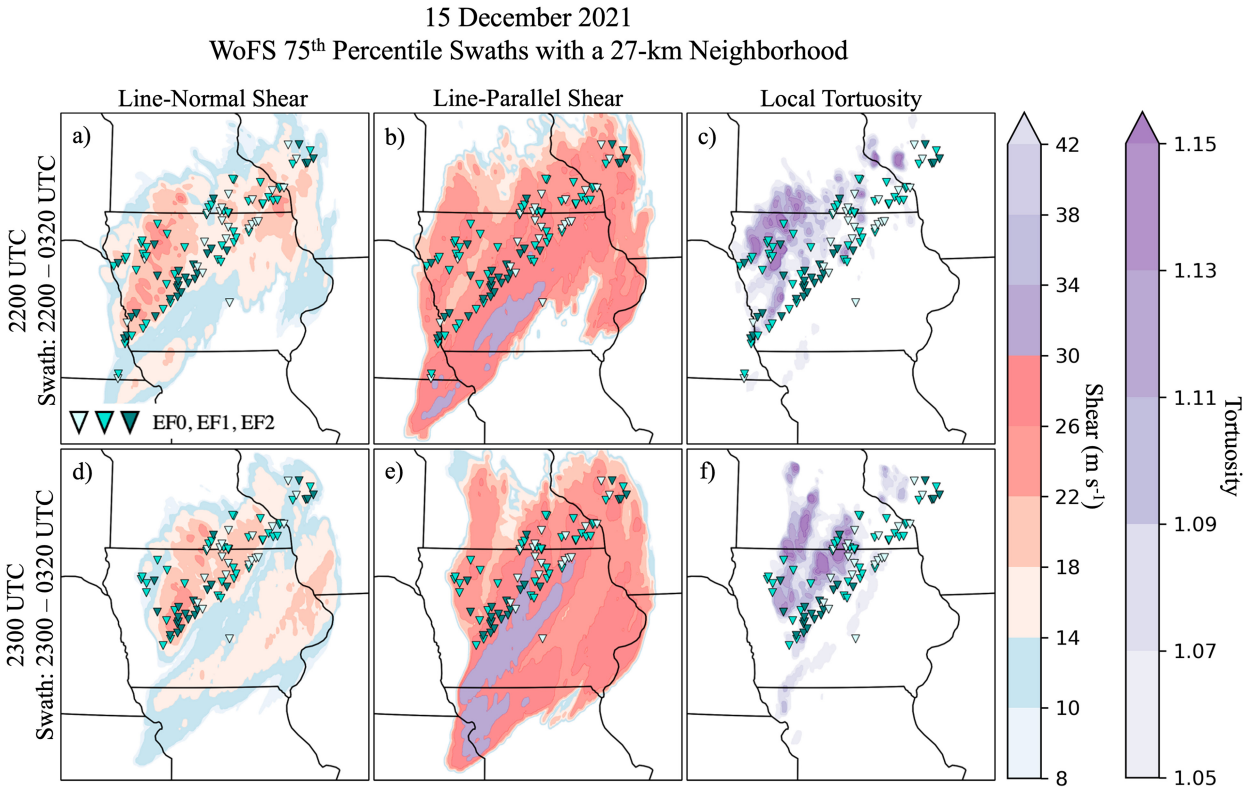


FIG. 6. WoFS 75th-percentile swaths of (left) LN03 shear, (center) LP01 shear, and (right) local tortuosity for the 15 Dec 2021 QLCS for the 2200–2300 UTC WoFS forecasts. Triangles represent the tornadoes reported during each swath time frame and are color coded by EF-scale intensity.

the previous high of 16 on 7 June 1984. Classified as a serial derecho (Johns and Hirt 1987; Squitieri et al. 2023a,b), this QLCS had strong forcing and multiple bowing segments along its convective line. Notably, it was the first documented derecho to occur in December anywhere in the United States, causing over $1 billion (U.S. dollars) in damages.

Only the 2200 and 2300 UTC WoFS forecasts are analyzed for this QLCS, as earlier forecasts depicted the QLCS as cellular convection rather than linear. This highlights a potential source of error in QTor forecasts: If the model fails to accurately predict the convective mode, particularly the development of a QLCS, then there will be no QTor.

At 2200 UTC, the LN03 shear forecast depicts a well-defined corridor in northern Iowa with values ranging from 14 to 26 m s^{-1}, encompassing most tornado reports associated with this QLCS (Fig. 6a). Similar to the 30 March 2022 case, this environment also features strong LP01 shear, with values exceeding 18 m s^{-1} (Fig. 6b). Areas with tortuosity greater than 1.07 are collocated with the majority of tornado reports in Iowa and southeastern MN (Fig. 6c).

The 2200 UTC QTor forecast reveals two primary swaths: a broad northern swath that aligns with most tornado reports and a shorter southern swath (Fig. 7a). The northern swath exhibits higher QTor values, ranging from 4 to 9, compared to the southern swath. This pattern is also evident in QTor probabilities of exceeding 2.5 (Fig. 7b). The southern swath initially reaches probabilities near 1.0, coinciding with two tornado reports, but then declines below 0.4 as the forecast progresses. Conversely, the northern swath maintains probabilities above 0.5 for most of the forecast duration, with lower probabilities toward the end of the swath, indicating lower confidence over time (Fig. 7b).

In the 2300 UTC forecast, the distinction between the two swaths becomes more pronounced. LN03 shear remains strongest in the northern swath, ranging from 14 to 26 m s^{-1}, and encompasses all but one tornado report, while the southern swath exhibits comparatively weaker LN03 shear (Fig. 6d). LP01 shear remains strong across both swaths, consistent with the 2200 UTC forecast (Fig. 6e), and tortuosity values above 1.07 continue to align with most tornado reports (Fig. 6f). Compared to the 2200 UTC forecast, the 2300 UTC QTor swath shows a narrower northern swath and a broader southern swath (Fig. 7c). The northern swath retains the highest QTor values and remains collocated with nearly all tornado reports, while the southern swath contains only one tornado report and is largely a false alarm (Fig. 7c). QTor probabilities of exceeding 2.5 remain elevated in both swaths but decrease toward the end of the forecast, indicating reduced confidence with increasing forecast time (Fig. 7d).

Overall, WoFS QTor forecasts identify the most favorable area for mesovortex tornadoes, aligning closely with documented tornado reports (Fig. 7). The tornadic phase for this

Brought to you by NOAA Library | Unauthenticated | Downloaded 09/14/26 03:13 PM UTC

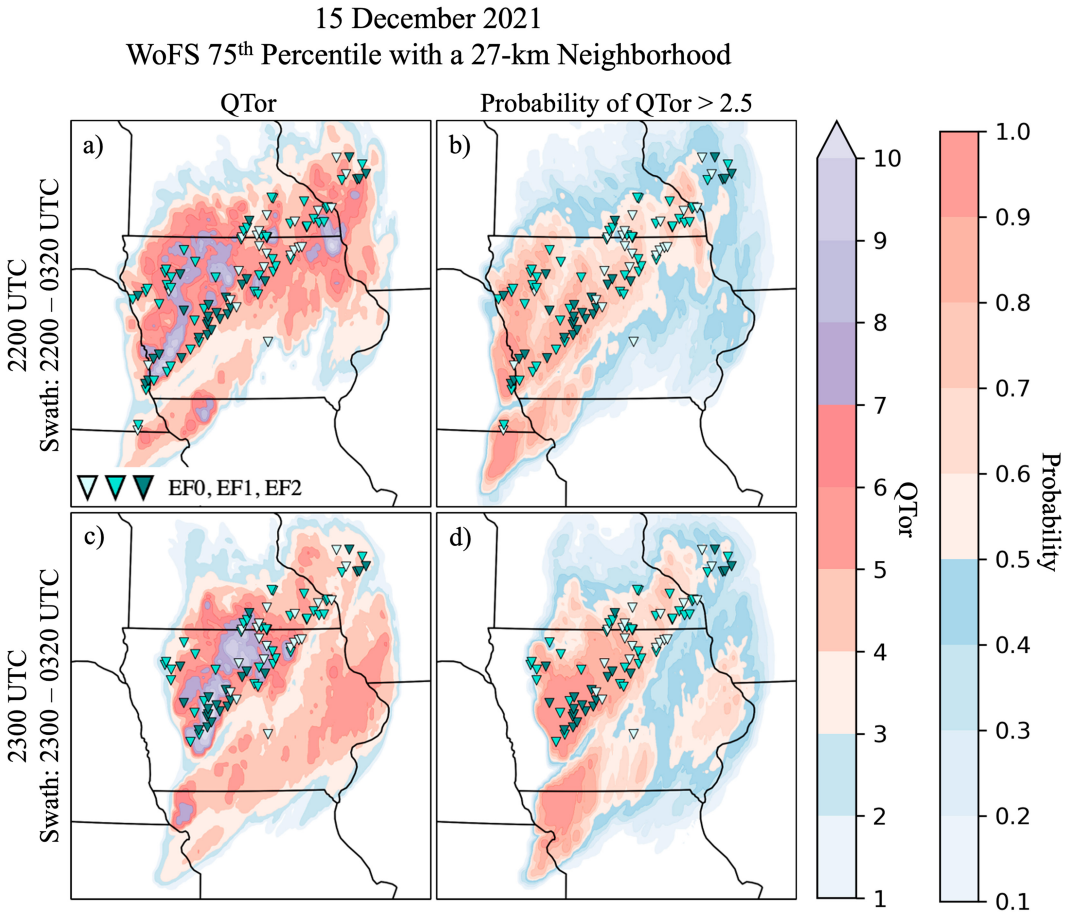


FIG. 7. As in Fig. 6, but for (left) QTor and (right) the probability that QTor will exceed 2.5.

QLCS was between 2205 and 0320 UTC. All tornadoes are well captured by the northern QTor swath, including those that occur later in the event, offering lead times between 4 and 5 h (Fig. 7). In contrast, the southern QTor swath is largely a false alarm, corresponding with only a single tornado report. However, QTor probabilities of exceeding 2.5 taper off quickly in space and time, indicating reduced tornado potential with increasing forecast time for the southern swath.

The WoFS maximum predicted swaths are compared to those derived from MRMS. The MRMS swaths are calculated using the same method as for WoFS but with one key difference: They use the observed MRMS leading line and compute QTor based on the near-storm environment from the 18-member WoFS ensemble. As a result, the MRMS swaths represent the probability of mesovortex tornadoes given the observed line orientation and the predicted mesoscale environment. In contrast, WoFS swaths represent the probability of mesovortex tornadoes occurring anywhere along the line, assuming WoFS captures sufficient variability in line orientation and evolution.

Compared to maximum predicted swaths in WoFS, MRMS depicts a narrower corridor of strong LN03 shear that closely matches the tornado reports (Fig. 8a). The MRMS LP01 shear swath features higher shear values, exceeding 30 m s^{-1}, concentrated south of the tornado reports compared to WoFS (Fig. 8b). Tortuosity also differs between MRMS and WoFS, with MRMS showing the highest tortuosity values primarily toward the end of the northern swath (Fig. 8c), whereas WoFS maintains more consistent alignment with tornado reports.

The MRMS QTor swath mirrors the LN03 shear swath, with a much narrower corridor of strong QTor values coinciding with the majority of tornado reports (Fig. 8d). Additionally, while MRMS does show a smaller swath of enhanced QTor to the south, it is not as broad or pronounced as in WoFS. Last, MRMS QTor probabilities exceeding 2.5 are 1.0 almost everywhere, correctly identifying the northern swath for tornado potential, but leading to false alarms in the southern swath (Fig. 8e).

The differences between MRMS and WoFS maximum parameter swaths can be attributed to variations in leading-line orientation and length (Fig. 9). At the beginning of the 2200 UTC forecast, the MRMS leading line is longer than the WoFS convective lines, causing the MRMS southern swath to extend farther south, while the northern swath remains narrower (Fig. 8). In contrast, after 0000 UTC, the WoFS leading lines become longer than the MRMS convective line, resulting in broader northern and southern swaths (Figs. 7 and 9).

Brought to you by NOAA Library | Unauthenticated | Downloaded 09/14/26 03:13 PM UTC

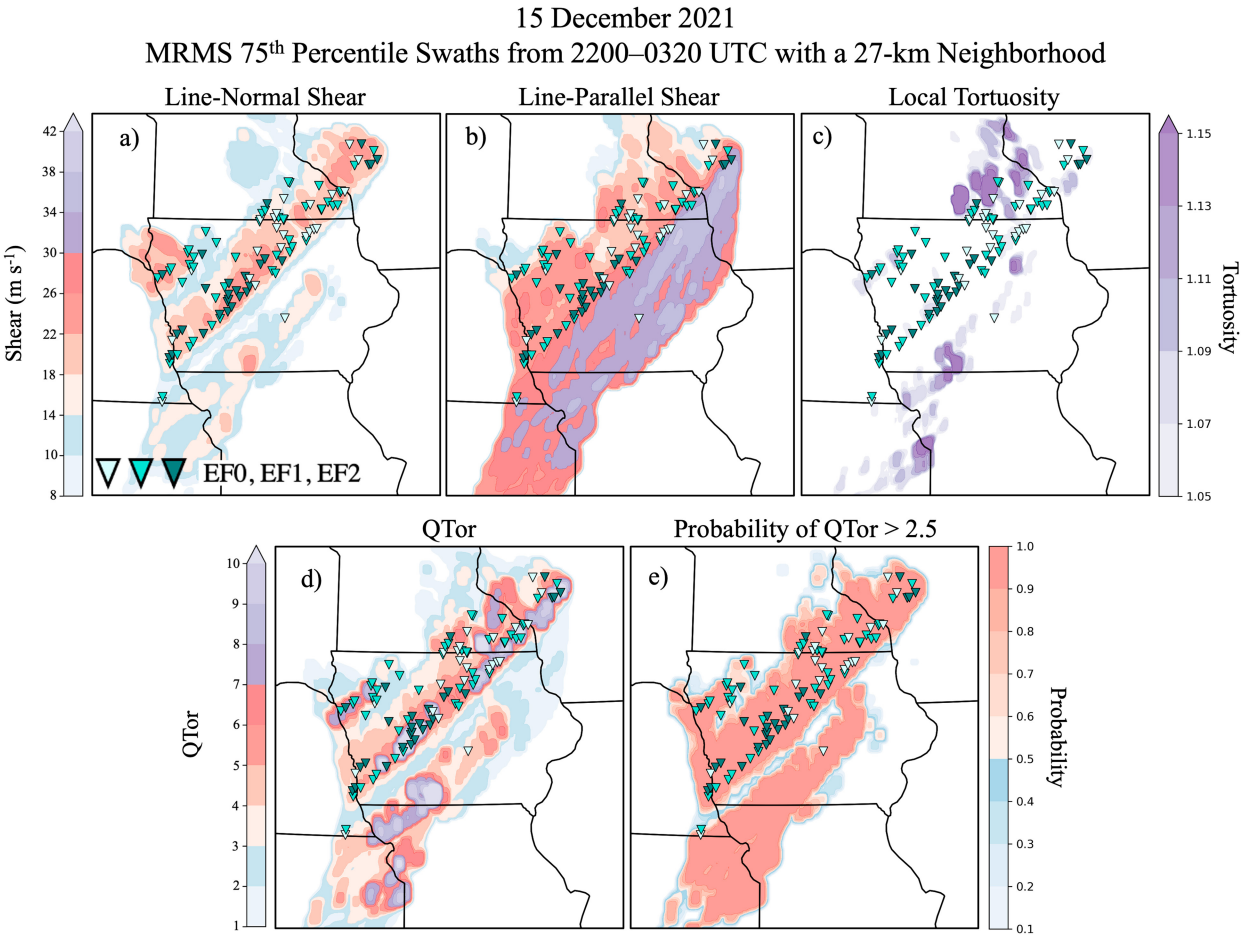


FIG. 8. MRMS 75th-percentile swaths from 2200 to 0320 UTC of (a) LN03 shear, (b) LP01 shear, (c) local tortuosity, (d) QTor, and (e) probability of QTor exceeding 2.5 for the 15 Dec 2021 QLCS. Note that when calculating QTor using just the MRMS line, any point on the line that exceeds 2.5 will produce a spot of 100% likelihood.

Additionally, as the QLCS evolves, differences in line orientation (Fig. 9) between the WoFS and MRMS leading lines contribute to discrepancies across all parameter swaths.

b. 30 March 2022 southeast QLCS

On 30 March 2022, a QLCS initiated along a dryline in southwest Oklahoma and northern Texas at approximately 0030 UTC. It moved through central Oklahoma and Texas before becoming disorganized around 0800 UTC. The convection continued eastward, reorganizing over Arkansas and Louisiana (LA) by 1700 UTC. The QLCS maintained a nearly meridional orientation, stretching from southern LA to central Illinois and Indiana. As the QLCS moved through LA, Mississippi (MS), and Alabama (AL), it produced numerous severe wind and tornado reports (Fig. 2). Most of those tornadoes were predominately rated as EF0 or EF1, with a few stronger tornadoes rated as either EF2 or EF3 (Fig. 2). Finally, the QLCS dissipated in Georgia around 1700 UTC 31 March 2022. This QLCS was chosen for this study as it exhibited a leading-stratiform, trailing-leading-line structure, and it developed in a HSLC environment typical of cool season southeastern U.S. severe weather environments (Sherburn and Parker 2014).

The 2000 UTC forecast for this QLCS shows minimal LN03 shear (Fig. 10a) but strong LP01 shear exceeding 26 m s^{-1} (Fig. 11b), consistent with the 0–1-km shear vector being predominately parallel to the QLCS's convective line. Strong LP01 shear is expected in the southeastern United States, as this area is characterized by a HSLC environment, known for having considerable low-level hodograph curvature and thus higher LP01 shear (Sherburn and Parker 2014; Sherburn et al. 2016; King et al. 2017; Chasteen and Koch 2022). This QLCS exhibits shorter-lived, localized bowing segments rather than a long-lived bow echo like in the other case studies. Therefore, as the QLCS evolves and develops bowing segments, the local tortuosity will become more important for tornado potential. Consequently, many of the tornado reports for this QLCS are collocated with pockets of enhanced tortuosity (Figs. 10 and 11).

At 2000 UTC, sufficient LN03 shear (Fig. 10a) and tortuosity (Fig. 10c) are present in western MS, aligning with tornado reports in this area. The corresponding QTor forecast (Fig. 11a)

Brought to you by NOAA Library | Unauthenticated | Downloaded 09/14/26 03:13 PM UTC

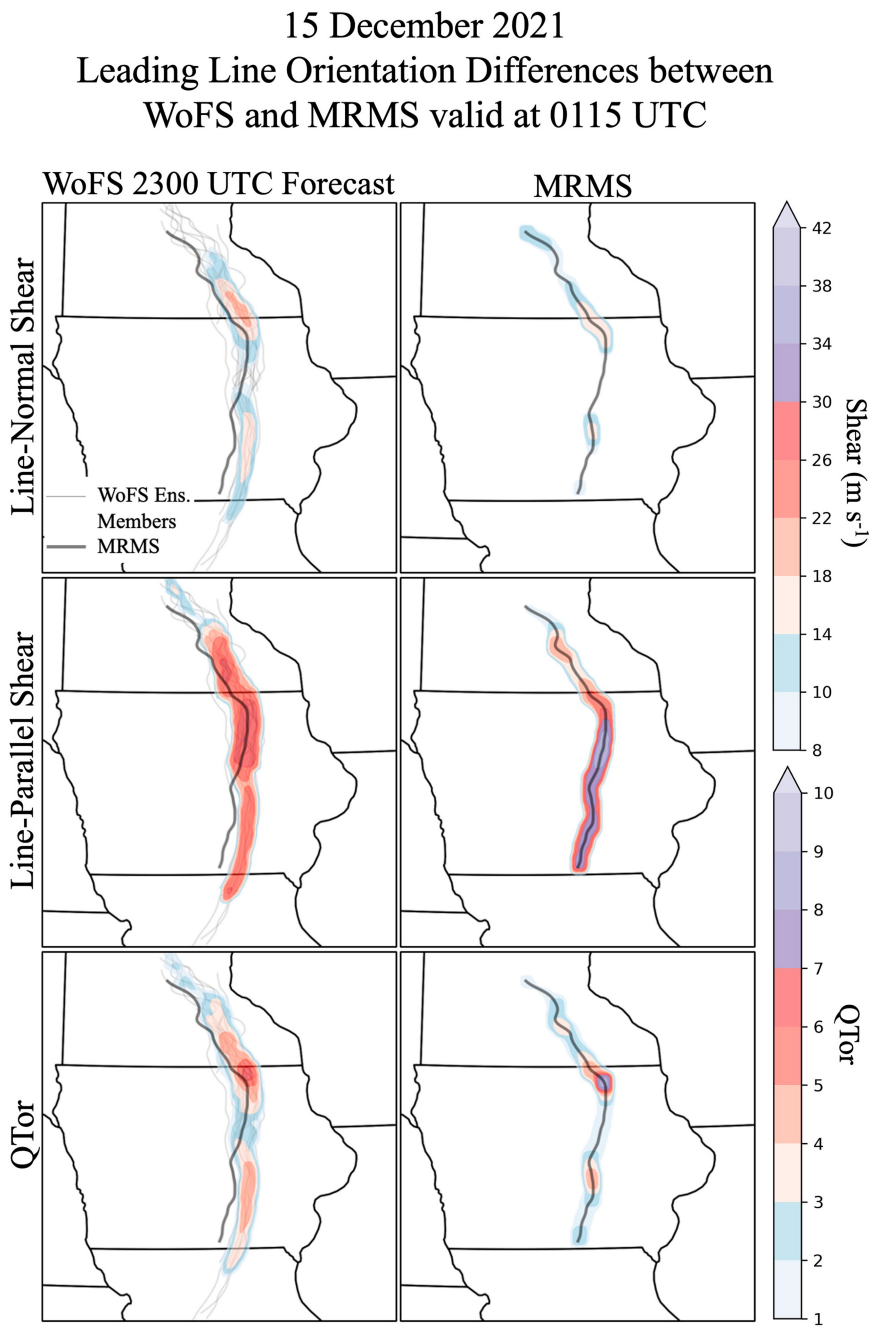


FIG. 9. (left) WoFS and (right) MRMS leading lines valid at 1150 UTC showing the differences in line orientation and length for the 15 Dec 2021 QLCS case. (top) LN03 shear, (middle) LP01 shear, and (bottom) QTor are shaded along the leading lines.

shows values between 3 and 8 where tornadoes occurred, with probabilities of QTor exceeding 2.5 above 0.5 (Fig. 11b). However, tornadoes in Tennessee (TN) and eastern MS are not captured by the QTor forecast (Fig. 11a) due to the absence of LN03 shear (Fig. 10a), leading to lower QTor values.

The 2100 UTC forecast for all maximum predicted parameter swaths (Figs. 10d–f) is similar to the 2000 UTC forecast. LN03 shear greater than 8 m s^{-1} is concentrated in northcentral MS, while LP01 shear exceeds 26 m s^{-1} everywhere in the swath. Increased values of tortuosity are present in the vicinity of many of the tornado reports, indicating the convective line is bowing outward in those locations (Fig. 10f). The QTor values (Fig. 11c) and probabilities (Fig. 11d) are highest in western MS, corresponding with the increase of LN03 shear and tortuosity in that area. There is also a small area of QTor between 3 and 5 along the border of central MS and AL but with low

Brought to you by NOAA Library | Unauthenticated | Downloaded 09/14/26 03:13 PM UTC

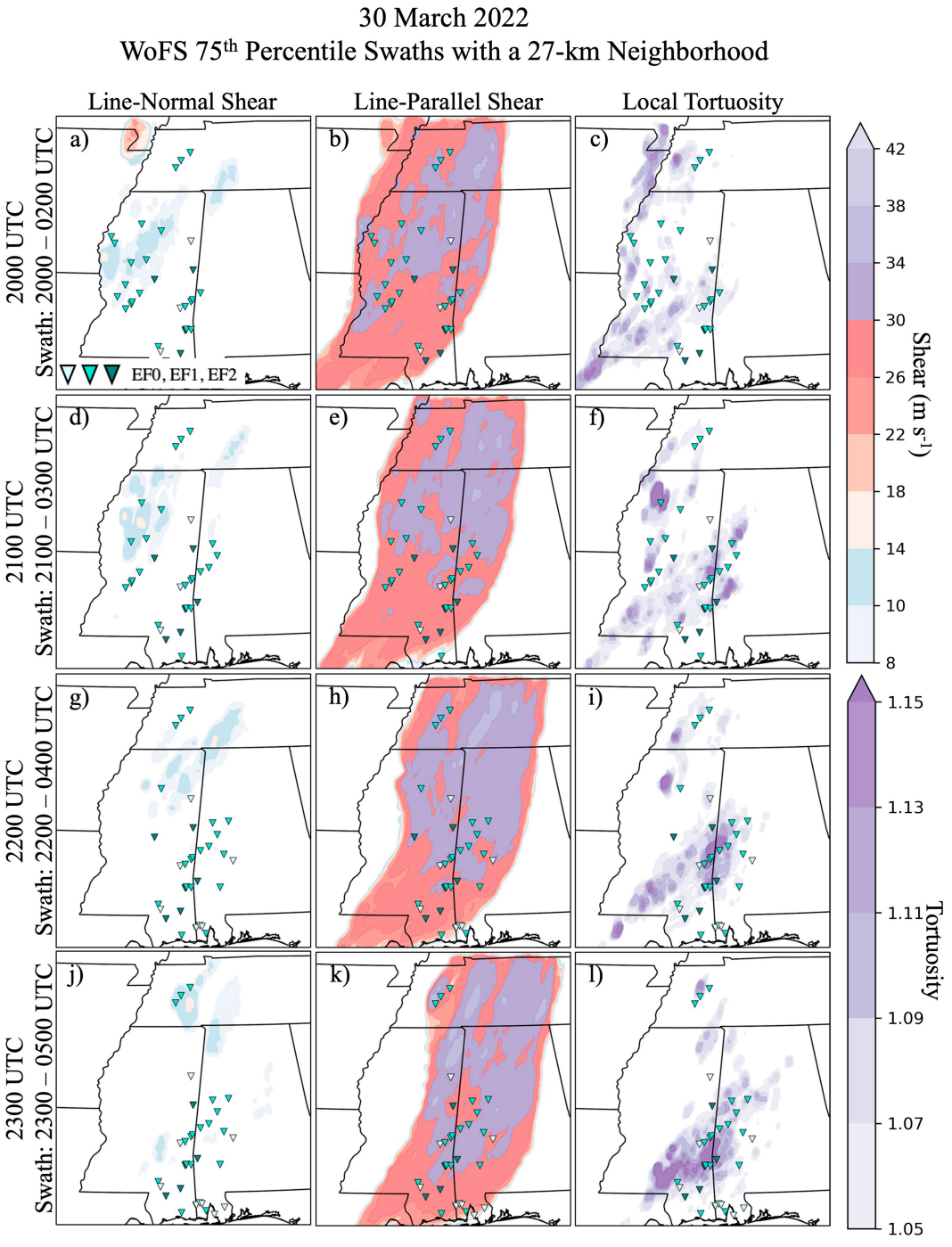


FIG. 10. As in Fig. 6, but for the 2000–2300 UTC forecasts for the 30 Mar 2022 QLCS.

probabilities. At the time of this forecast, this small spot of QTor along the MS/AL border is a 4-h forecast. While it has low confidence, QTor is picking up on a signal that aligns with the tornado reports observed in this area.

For the 2200 UTC forecast, LN03 shear above 8 m s^{-1} is concentrated in northern MS/AL and TN (Fig. 10g). On the other hand, LP01 shear greater than 30 m s^{-1} has increased in area (Fig. 10h), compared to the 2100 and 2000 UTC forecasts. Similar to the 2000–2100 UTC forecast, increased values of tortuosity coincide with the majority of the tornado reports, especially along the central border of MS/AL (Fig. 10i). For QTor, there are increased values in north-central MS and southern TN that correspond to the increases in LN03 shear (Fig. 11e). As first observed in the 2100 UTC forecast, there is a small swath of QTor

Brought to you by NOAA Library | Unauthenticated | Downloaded 09/14/26 03:13 PM UTC

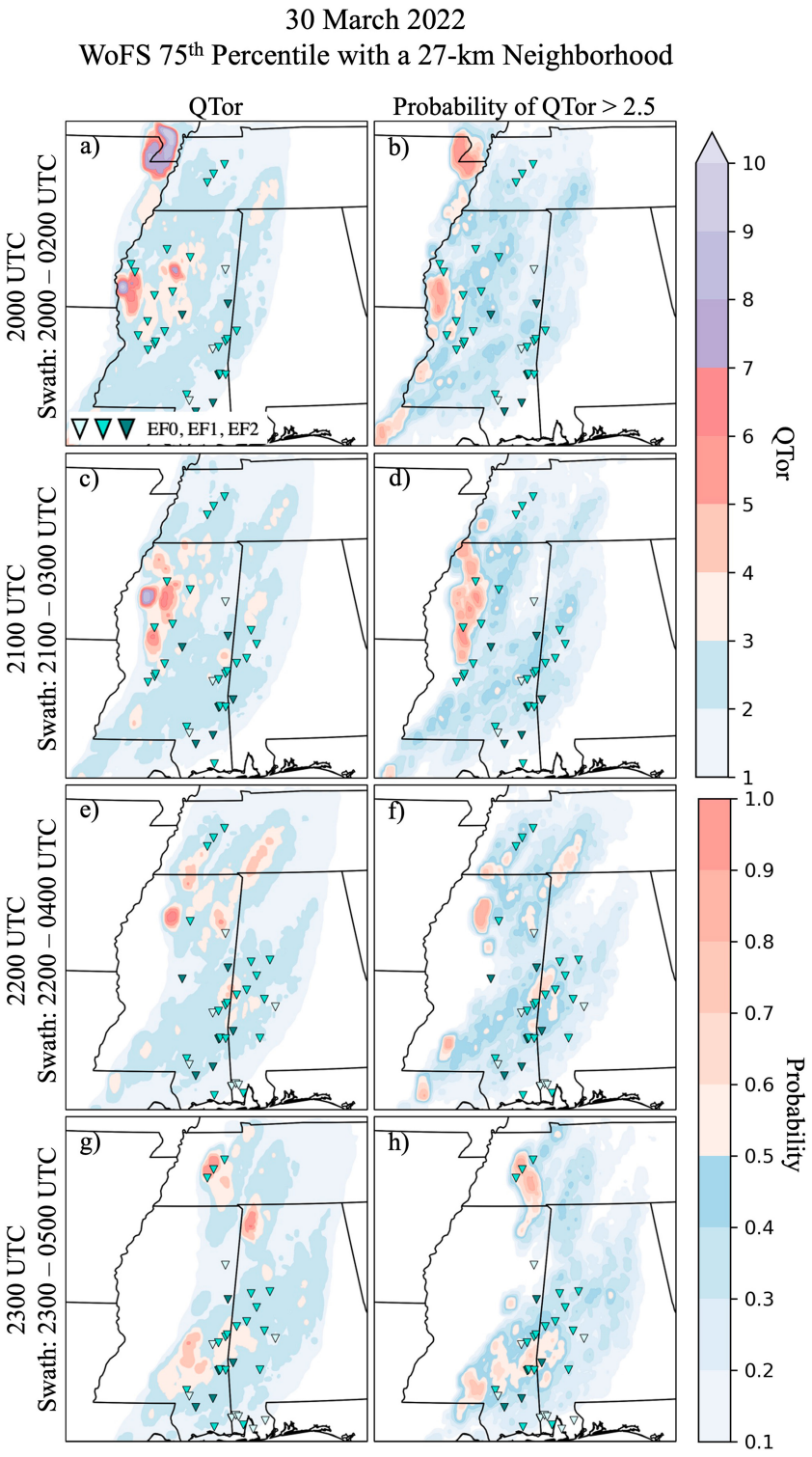


FIG. 11. As in Fig. 7, but for the 30 Mar 2022 QLCS.

Brought to you by NOAA Library | Unauthenticated | Downloaded 09/14/26 03:13 PM UTC

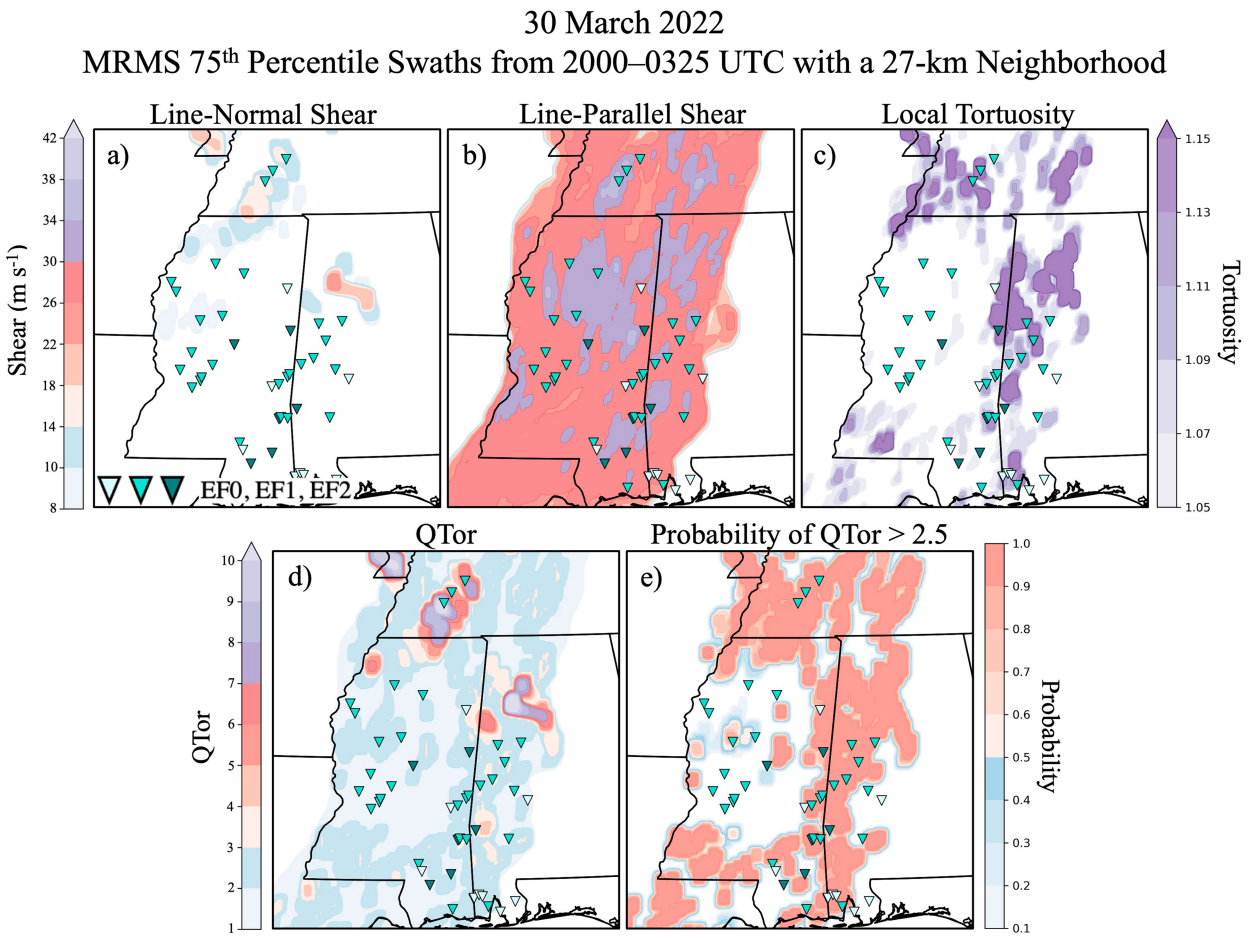


FIG. 12. As in Fig. 8, but for the 30 Mar 2022 QLCS.

values between 3 and 5 along the central border of MS/AL (Fig. 11e) but now with higher probabilities (Fig. 11f). Though enhanced QTor values do not encompass the full swath of tornado reports in this area, the enhanced values provide an advanced indication that tornadic mesovortices are relatively more likely along this portion of the QLCS.

By 2300 UTC, LN03 shear is minimal throughout the domain (Fig. 10j) with a small bull's-eye in TN coinciding with tornado reports. LP01 shear remains above 26 m s^{-1} throughout the swath (Fig. 10k). Tortuosity surpasses 1.11 in TN, southern MS, and west-central MS, aligning well with tornado reports (Fig. 10l). QTor closely mirrors the tortuosity forecast (Fig. 11g), reflecting the expected link between bowing segments and tornado potential. As a convective line bows or surges outward, enhanced convergence leads to a higher tornado potential, making these bows a common location for tornadogenesis and a key ingredient in the 3IM (Fig. 1; Przybylinski 1995; Atkins et al. 2005; Xu et al. 2015). The QTor probabilities increase near the tornadoes reported in TN and central MS/AL, improving confidence compared to previous forecasts (Fig. 11h).

Comparing WoFS and MRMS swaths (Fig. 12), MRMS LN03 shear (Fig. 12a) is minimal in TN and northwest MS, aligning with WoFS values (Figs. 10a,d,g,j). However, MRMS shows an LN03 shear increase in north-central AL that is not present in WoFS and does not correspond with any tornado reports. LP01 shear is consistent between MRMS (Fig. 12b) and WoFS (Figs. 10b,e,h,k), exceeding 26 m s^{-1} throughout the swath. The MRMS tortuosity swath (Fig. 12c) is similar to WoFS (Figs. 10c,f,i,l), except for a region of low values in western MS. There are also higher tortuosity values in northeastern AL, collocated with a maximum in LN03 shear. These maxima in LN03 shear and tortuosity are attributable to individual cells that initiate upstream and merge into the line. These mergers cause local areas of greater-line tortuosity in the leading line that increase values of LN03 shear and tortuosity. One of these bumps can be observed in the MRMS leading line at 0200 UTC in Fig. 2. The MRMS QTor swath (Fig. 11d) highlights values between 5 and 10 near the TN tornadoes, though with many other high QTor regions being false alarms. MRMS QTor probabilities of exceeding 2.5 (Fig. 12e) are 1.0 across the swath, capturing some of the tornado reports but also resulting in a large number of false alarm areas. Since there is only the MRMS leading line to calculate QTor from, any point on that line exceeding QTor of 2.5 will generate a spot of 100% likelihood.

Brought to you by NOAA Library | Unauthenticated | Downloaded 09/14/26 03:13 PM UTC

The 30 March 2022 QLCS was selected as a representative HSLC event in the southeastern United States. The tornadic phase for this QLCS occurred from 2019 to 0450 UTC, within the domain of interest. The most pronounced areas of enhanced QTor typically occurred within the first 2–3 h, with both QTor and exceedance probabilities decreasing beyond that window (Fig. 11). Although QTor values and probabilities exceeding 2.5 were generally lower than in other case studies, QTor still identified portions of the QLCS with higher tornado potential that were collocated with tornado reports. However, large areas of false alarms remained, primarily owing to elevated tortuosity along bowing segments that were incorrectly predicted (e.g., cell mergers). This case highlights the need for further refinement of QTor thresholds using a broad range of HSLC events. Future improvements may also incorporate region-specific shear thresholds to better predict QLCS tornado potential in HSLC environments across the southeastern United States.

c. 12 May 2022 Midwest derecho

The 12 May 2022 QLCS developed along a cold front around 1500 UTC in southwestern Kansas. Initially, the convection consisted of disorganized cells, which grew rapidly upscale to become quasi-linear over southern Nebraska by 1830 UTC. The system moved northeast, evolving into a classic leading-line, trailing-stratiform structure by 2200 UTC. It persisted until reaching east-central MN around 0200 UTC. Accordingly, the 2000–2300 UTC WoFS forecasts are analyzed for this study to examine the LN03 shear, the LP01 shear, local tortuosity, and their influence on QTor forecasts.

This QLCS, also classified as a derecho (Johns and Hirt 1987), caused over a billion dollars in damage due to widespread straight-line winds and 31 confirmed tornadoes, primarily in northeast South Dakota (SD) and west-central MN. Most tornadoes were rated EF0–EF1, though five EF2 tornadoes caused extensive damage in eastern SD and west-central MN (Fig. 2).

This case was selected for this study due to its high-impact nature, producing both destructive straight-line winds and tornadoes indicative of embedded mesovortices. Additionally, it serves as a classic warm-season Midwest case, which makes it relevant to understand how QTor performs for this common type of QLCS. The QLCS also exhibited two distinct leading-line orientations (Fig. 2): a northern segment aligned approximately east–west and a southern segment oriented more north–south. These differing orientations allow for a comparative analysis of LN03 and LP01 shear relative to the leading-line orientation and how it influences mesovortex tornado development.

Starting with the 2000 UTC forecast, a 5-h and 20-min swath of predicted maximum LN03 shear exceeding 14 m s^{-1} encompasses the majority of the tornado reports associated with this storm (Fig. 13a). LP01 shear spans a broader area than LN03 shear but exhibits similar magnitudes also coinciding with reported tornadoes (Fig. 13b). Additionally, local tortuosity values (Fig. 13c) indicate ample curvature along the leading line as it traverses the region.

Since both LN03 and LP01 shear exceed the QTor equation thresholds [Eq. (6)], QTor values range from 3 to 7 in the predicted maximum swath, aligning with the tornado reports (Fig. 14a). This northern QTor swath corresponds with probabilities of QTor exceeding 2.5 being greater than 0.5 (Fig. 14b), indicating that more than half of the WoFS ensemble members identify this area as favorable for mesovortex tornado formation.

Subsequent, shorter lead-time forecasts initialized at 2100 (Figs. 13d–f), 2200 (Figs. 13g–i), and 2300 (Figs. 13j–l) UTC are consistent with the 2000 UTC forecast. The most substantial change is in the LN03 shear field, where areas of magnitudes exceeding 22 m s^{-1} expand to include more tornado reports. This increase in LN03 shear corresponds to higher QTor values (Figs. 14c,e,g), with some areas exceeding 7. The QTor probabilities also increase (Figs. 14d,f,h), covering more tornado reports compared to the 2000 UTC forecast (Fig. 14b). Therefore, confidence in this portion of the QLCS-producing mesovortex tornadoes strengthens with subsequent forecast initializations.

The MRMS swaths for LN03 shear, QTor, and probability of QTor exceeding 2.5 (Figs. 15a,d,e) resemble those from WoFS, aligning with most of the reported tornadoes. However, the MRMS swaths show a northwestern offshoot through SD and North Dakota that is not associated with tornado reports and is not present in the predicted WoFS QTor swaths (Fig. 15). Further inspection reveals this offshoot results from a limitation in the leading-line object identification process (Fig. 16). The northern portion of the MRMS leading line shows a sharp bow, also coinciding with high QTor values due to the increase in curvature (Fig. 16). However, composite reflectivity indicates this bowing segment in the MRMS leading line is distinct from the QLCS and is made up of disorganized convection to the northwest of the QLCS.

Additionally, MRMS shows a clear slot in LP01 shear, with values around 10–14 m s^{-1} near the reported tornadoes in northeast SD and western MN (Fig. 15b). While this feature is also visible in the 2100 (Fig. 13e) and 2200 (Fig. 13h) UTC WoFS forecasts for LP01 shear, it is smaller and less prominent compared to MRMS. The low LP01 shear values in MRMS arise because this portion of the QLCS is oriented more east–west than in WoFS (Fig. 17), meaning all of the shear is LN relative to the MRMS leading line. In contrast, the WoFS leading lines are oriented more northwest–southeast in this area resulting in a more substantial LP component to the shear, which is not observed in MRMS (Fig. 17). This explains why a clear slot of very low LP01 values appears in MRMS but not in WoFS.

Overall, the 12 May 2022 QTor forecasts highlighted the portion of the QLCS associated with the greatest apparent risk for mesovortex tornadoes, based on the observed reports from this day. The first WoFS forecast initialized at 2000 UTC suggested the area most favorable for mesovortex tornado development also aligned with the observed tornado reports. Since the tornadic period for this QLCS was between 2240 and 0050 UTC, the 2000 UTC forecast provided an estimated lead time of 2.5–4.5 h. Subsequent forecasts refined this area

Brought to you by NOAA Library | Unauthenticated | Downloaded 09/14/26 03:13 PM UTC

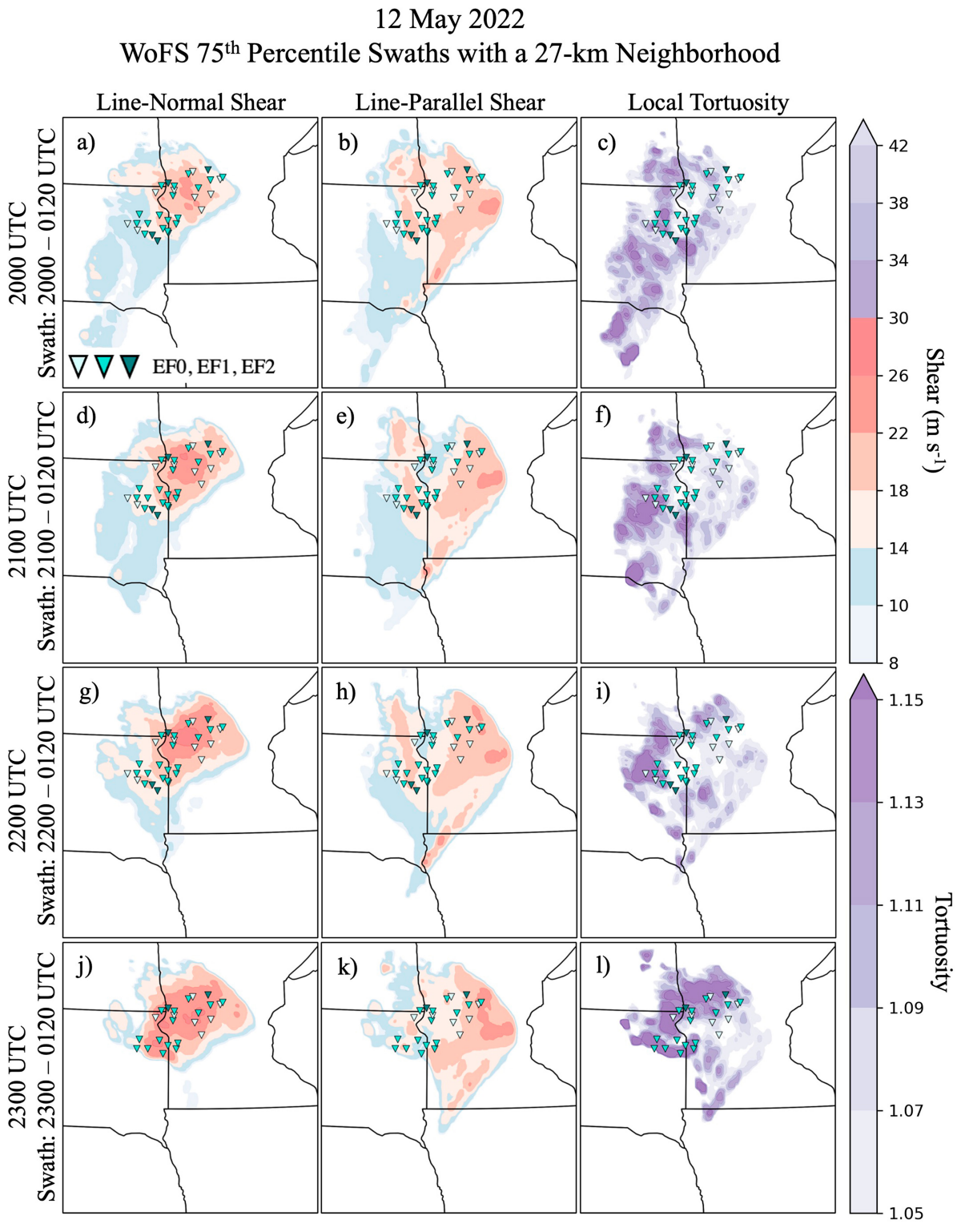


FIG. 13. As in Fig. 6, but for the 2000–2300 UTC forecasts for the 12 May 2022 QLCS.

Brought to you by NOAA Library | Unauthenticated | Downloaded 09/14/26 03:13 PM UTC

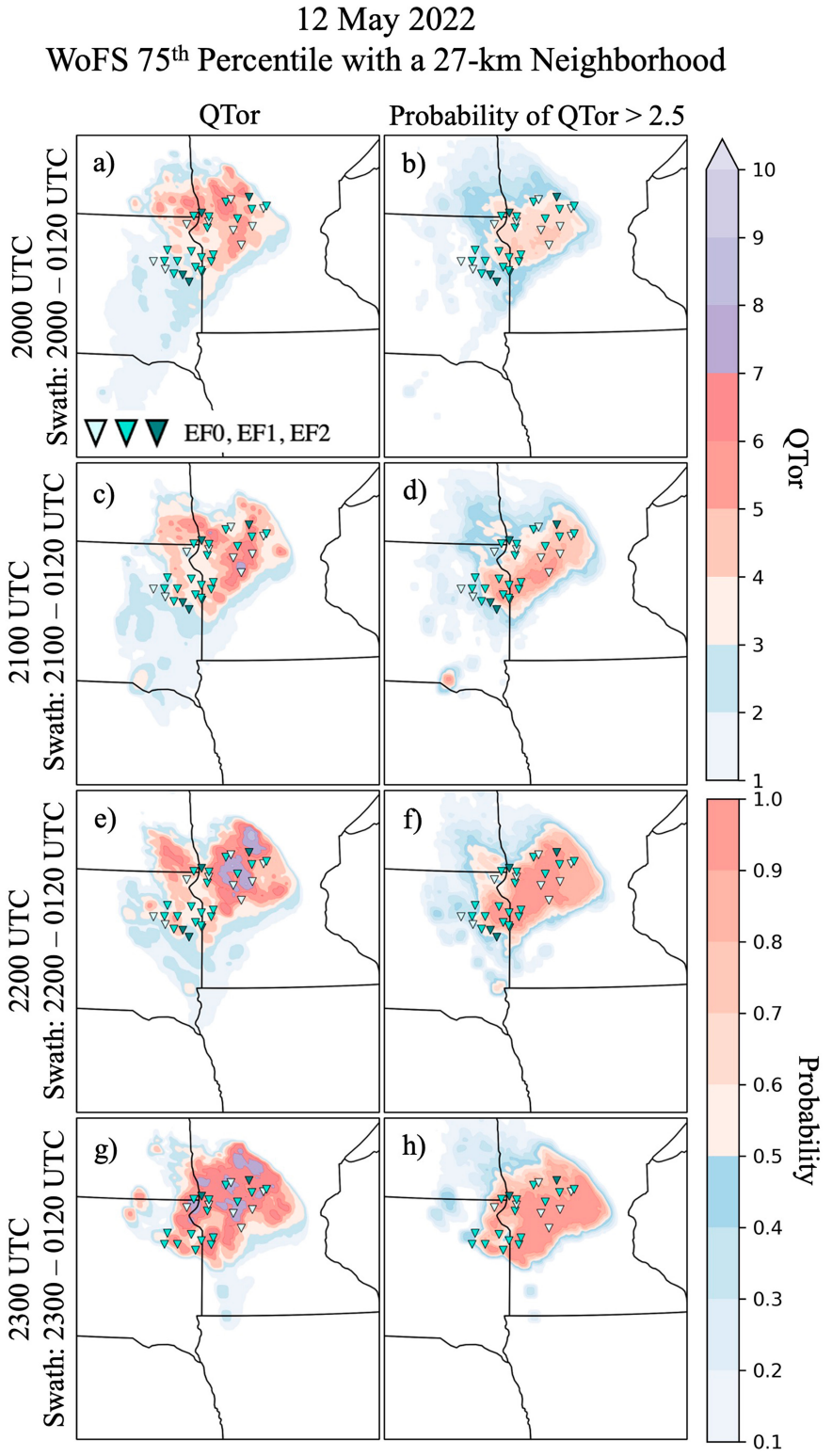


FIG. 14. As in Fig. 7, but for the 12 May 2022 QLCS.

Brought to you by NOAA Library | Unauthenticated | Downloaded 09/14/26 03:13 PM UTC

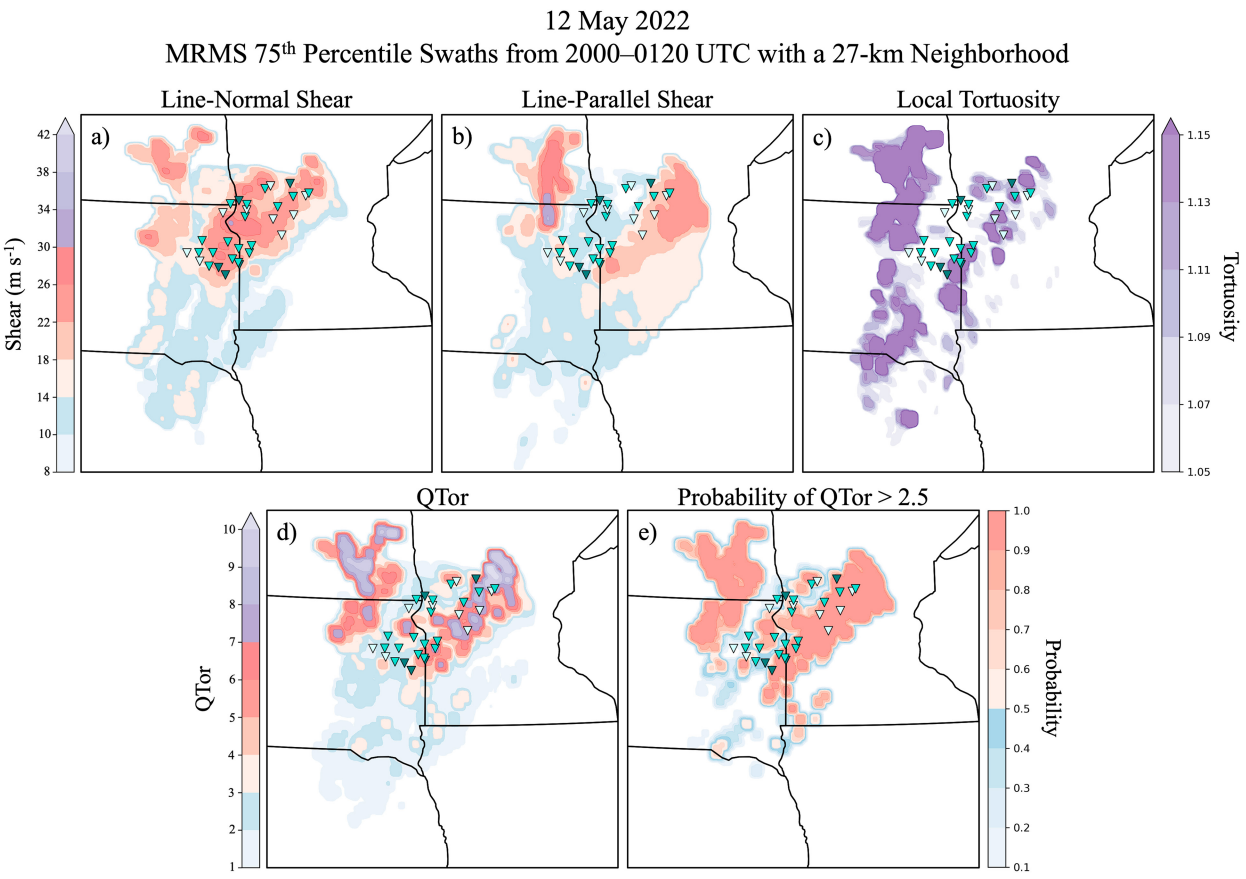


FIG. 15. As in Fig. 8, but for the 12 May 2022 QLCS.

and increased the confidence for tornado development (seen in QTor exceedance probabilities; Figs. 14b,d,f,h).

d. 19 May 2024 null case

The 19 May 2024 QLCS was selected as a null case to subjectively analyze QTor capabilities in a system that produced little to no tornadoes. Convection initiated at approximately 1830 UTC in west-central Kansas and organized into a linear structure by 2230 UTC. Although a few tornadoes occurred prior to 2300 UTC, these are excluded from consideration as they fall outside the analysis window selected for this study.

By 0000 UTC, the QLCS had developed a prominent bow echo and an intense northern bookend vortex. From 2300 to 0100 UTC, the system remained nontornadic, after which it produced three weak tornadoes: one at 0119 UTC and two after 0200 UTC (Fig. 2). By 0300 UTC, the QLCS reached the edge of the WoFS domain and began to weaken into disorganized convection. Accordingly, only the 2300 and 0000 UTC WoFS forecasts are analyzed, with the evaluation period ending at 0300 UTC for both forecasts. This setup provides a 2-h nontornadic period (2300–0100 UTC) followed by a 2-h tornadic period (0100–0300 UTC), making it a useful null case for evaluating QTor under conditions of minimal tornadic activity.

In the 2300 UTC WoFS forecast, LN03 shear is weak, with only localized increases near the reported tornadoes (Fig. 18a). LP01 shear, in contrast, exceeds the 8 m s^{-1} threshold across the entire swath (Fig. 18b). Tortuosity greater than 1.05 is also present near the reported tornadoes (Fig. 18c). Correspondingly, QTor values remain low, generally 1–2, but with isolated increases to 2–3 near the EF0 tornadoes (Fig. 19a). Probabilities that QTor will exceed 2.5 are zero across most of the swath, increasing slightly to 0.1–0.3 only near the EF0 tornado reports (Fig. 19b).

The 0000 UTC WoFS forecast shows a similar pattern. LN03 shear remains below the 10 m s^{-1} threshold except near the later tornadoes (Fig. 18d). LP01 shear resembles the previous forecast but extends farther south to include the EF1 tornado (Fig. 18e). Local tortuosity is less widespread than in the 2300 UTC forecast, with increases confined mainly near the three tornado reports, indicating the formation of bowing segments before tornadogenesis occurs (Fig. 18f). The QTor values again range from 1 to 2 across most of the swath but increase to 3–5 near the tornadoes, with maxima slightly displaced east of the reports (Fig. 19c). The QTor exceedance probabilities follow a similar pattern, with the greatest confidence (60%) east of the EF1 tornado report (Fig. 19d).

MRMS swaths from 2300 to 0300 UTC closely resemble WoFS. LN03 shear is below 8 m s^{-1} in most of the swath,

Brought to you by NOAA Library | Unauthenticated | Downloaded 09/14/26 03:13 PM UTC

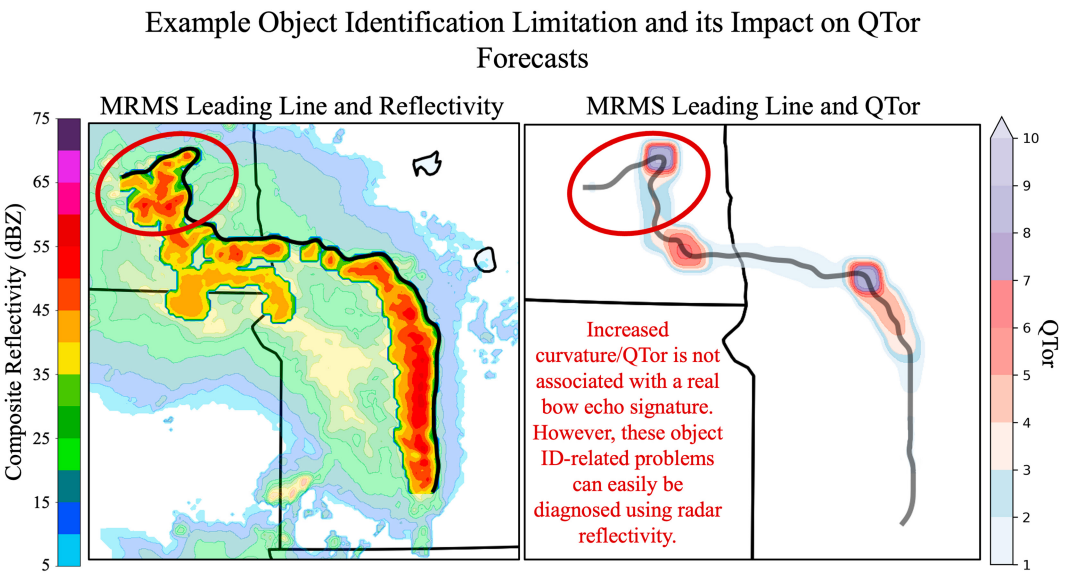


FIG. 16. (left) Composite reflectivity and (right) QTor along the MRMS leading line showing a limitation of the object identification methods used in this study. Opaque reflectivity denotes the MRMS QLCS object, while the transparent reflectivity represents the full composite reflectivity field. While the MRMS leading line shows a bowing segment (red circle), this is associated with trailing cellular convection rather than the QLCS. While this is a limitation of object-based identification methods, these problems can be diagnosed by viewing reflectivity with QTor forecasts.

with values greater than the 10 m s^{-1} threshold concentrated near the tornado reports (Fig. 20a). LP01 shear has a similar extent to the 2300 UTC WoFS forecast but is slightly stronger near the tornadoes (22–26 m s^{-1}; Fig. 20b). Tortuosity is also slightly higher, with localized maxima exceeding 1.15 (Fig. 20c). MRMS QTor values are similar in extent and magnitude, with broad areas of 1–2 values and maxima of 3–5 near the tornadoes (Fig. 20d). MRMS QTor exceedance probabilities are also similar in location and spatial extent to WoFS, with maxima to the west of the reported tornadoes (Fig. 20e). The primary difference is the spatial displacement of the QTor maxima compared to the tornado reports: MRMS places the maxima to the west of the tornadoes, while WoFS places them to the east. This offset may be attributable to QLCSs in WoFS moving faster than observed (not shown).

In summary, both WoFS and MRMS have low QTor values and negligible exceedance probabilities during the QLCS's nontornadic phase, with localized increases only near the observed tornadoes. This case highlights QTor's ability to reflect the low tornado risk during quiescent periods while signaling enhanced potential during tornadic phases. The observed tornadoes develop after 0100 UTC, so QTor provides 1–2 h of lead time. These results are encouraging, but additional null cases are needed to fully assess QTor's capability in distinguishing tornadic from nontornadic QLCS environments.

4. Discussion of limitations

QTor shows promise in identifying regions along QLCSs that are most favorable for mesovortex tornado development, with lead times extending up to 3 h. While quantitative verification is still needed, forecasts that depict large, contiguous areas of elevated QTor values, especially when those areas remain consistent across successive model runs, can help increase forecaster confidence in pinpointing specific QLCS segments most conducive to tornado formation. As with any derived forecasting parameter, particularly in a proof-of-concept study, QTor is subject to several inherent limitations that must be addressed through continued evaluation and refinement.

A primary limitation is the lack of generalizability across the full spectrum of QLCS environments and line orientations due to the small number of cases analyzed. This study evaluates QTor's forecast capabilities across three events representing distinct seasonal and regional QLCS regimes: cold-season, warm-season, and southeastern U.S. setups, as well as a null case. While these cases provide a useful initial test, the limited sample precludes robust statistical evaluation and may not fully capture the variability in QLCS structure or environmental shear profiles. Future work will address this by applying QTor to a larger, more diverse set of QLCS cases.

In addition, because this study is intended as a proof of concept with a small number of cases, verification was conducted subjectively/qualitatively. This approach is both feasible and informative, providing early insight into how the algorithm behaves across different QLCS environments and whether the methods function as intended. While subjective assessment cannot fully quantify forecast skill, it highlights aspects that may require refinement and provides a first look at algorithm functionality. Future application to a larger QLCS dataset will incorporate objective, quantitative verification metrics to rigorously evaluate QTor's skill and performance.

Another limitation is that forecast errors inherent to WoFS can impact QTor's accuracy. WoFS has been shown to misrepresent the leading line's orientation (e.g., 12 May 2022;

Brought to you by NOAA Library | Unauthenticated | Downloaded 09/14/26 03:13 PM UTC

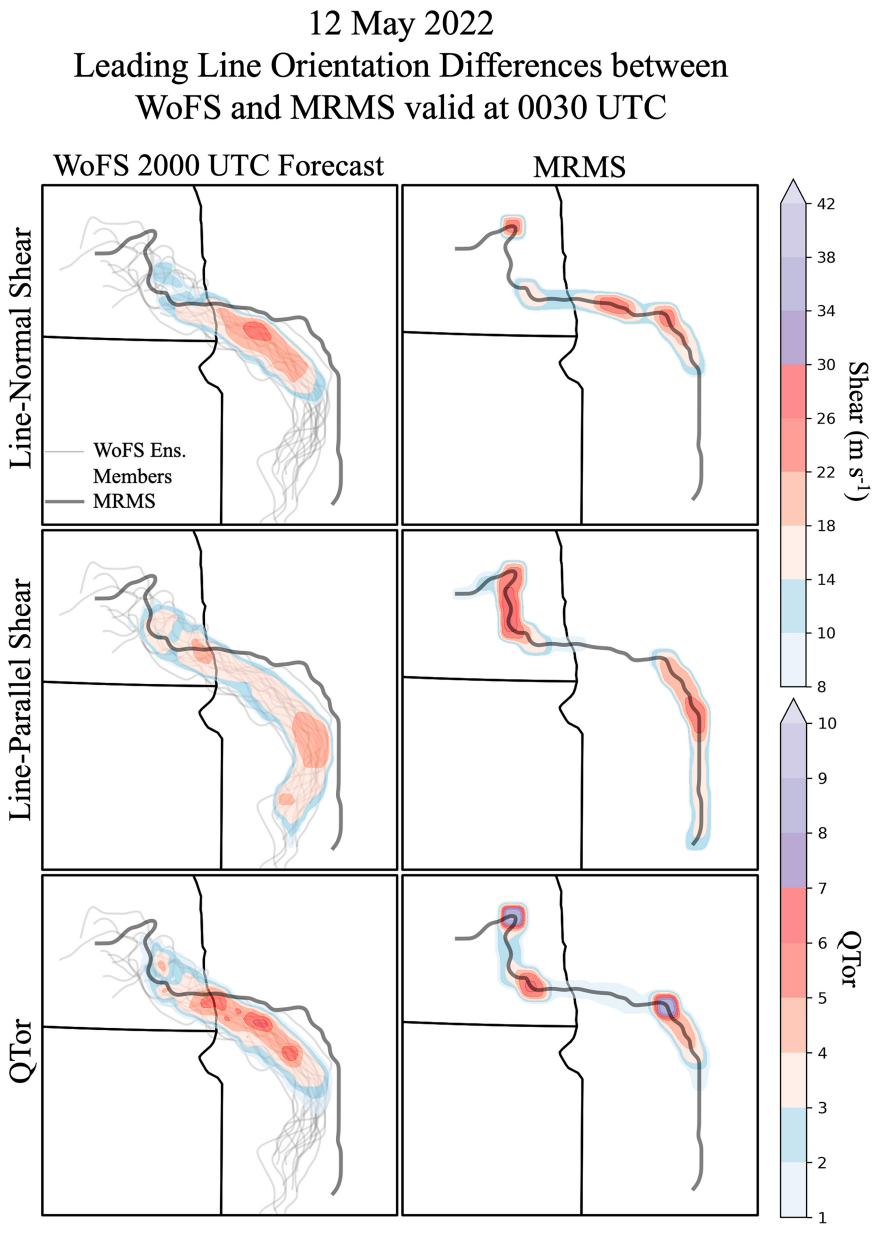


FIG. 17. As in Fig. 9, but for the 12 May 2022 case valid at 0030 UTC.

Fig. 17) and spatial extent (e.g., 15 December 2021; Fig. 9), which directly affects system-relative shear calculations. Previous work has documented a tendency for WoFS to overpredict the strength of the northern bookend vortex and rear-inflow jet, often causing QLCSs to bow excessively (Britt et al. 2024). This artificial bowing alters leading-line geometry, subsequently impacting QTor calculations. In more extreme instances, WoFS may fail to predict the correct storm mode (e.g., 15 December 2021), precluding QTor calculation. Although not directly addressed in this study, errors in the near-storm environment, such as inaccuracies in shear direction or magnitude, may also degrade QTor performance.

Additional limitations arise from the object and leading-line identification algorithms. These automated algorithms can struggle in complex convective scenarios. For example, on 12 May 2022, trailing cellular convection resulted in errors in leading-line orientation (Fig. 16), while on 30 March 2022, cell mergers caused the algorithm to erroneously identify bowing segments. These structural complexities can produce spurious QTor signals or mask actual tornado-favorable segments. As a result, in operational settings, forecasters are encouraged to interpret QTor forecasts in conjunction with observed radar reflectivity (when available) to identify errors and adjust their interpretation of the forecast accordingly.

Brought to you by NOAA Library | Unauthenticated | Downloaded 09/14/26 03:13 PM UTC

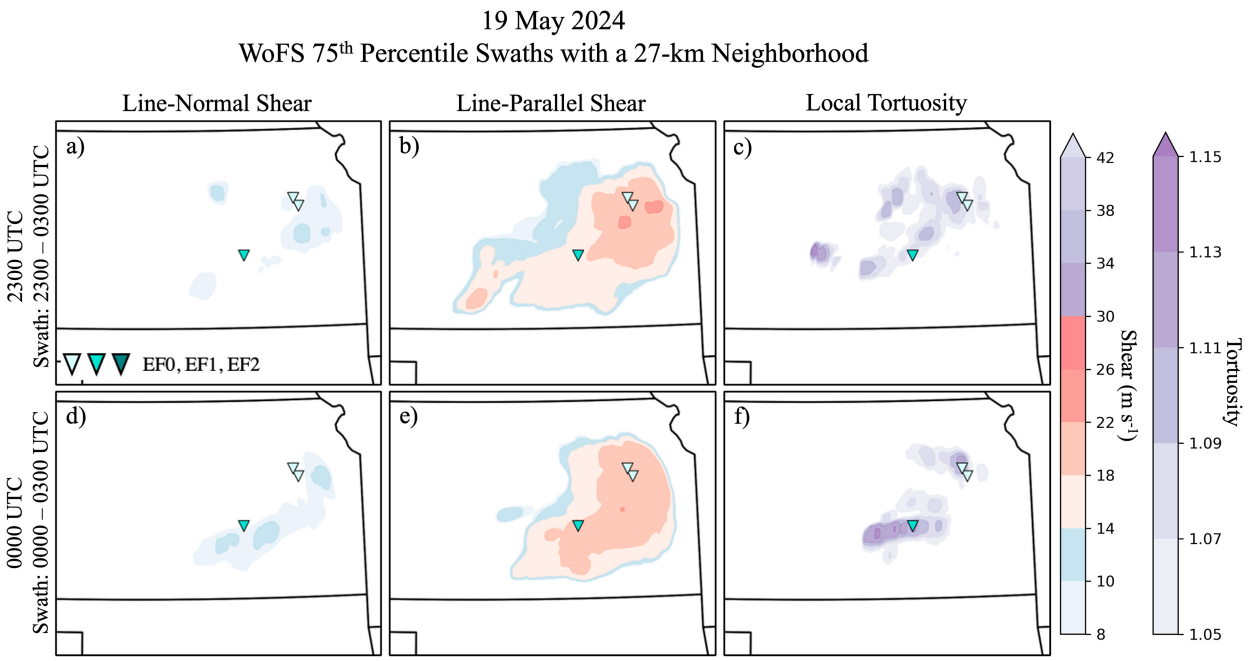


FIG. 18. As in Fig. 6, but for the 2300–0000 UTC forecasts for the 19 May 2024 QLCS.

The final limitation of the current QTor algorithm is that the SM calculation is not yet fully automated. Full automation is essential for operational implementation, particularly with rapidly updating ensemble systems like WoFS. To address this, ongoing work is exploring the use of QLCS object centerlines (Britt et al. 2024) to track mean SM over time. Using a KDTree nearest-neighbor approach, each point along the object's centerline is matched to the nearest point of the centerline at the next time step. Taking the average of the storm speed and direction from each point gives a mean SM vector for the entire QLCS. This SM vector is then used to identify the leading edge of each QLCS object.

Initial tests show that this method produces SM vectors consistent with manual estimates. While some errors are expected in cases with messy or disorganized centerlines, the algorithm only requires a general SM vector (i.e., which mathematical quadrant the motion lies in) to identify the leading lines, making it robust to such issues. More extensive testing will be conducted prior to fully integrating this step into the automated QTor algorithm.

5. Summary and conclusions

The current QLCS tornado warning paradigm used operationally, 3IM, leans heavily on system balance modulated by LN shear and is applied subjectively along with numerous radar-derived "nudgers." This study sought to develop and test a parameter which evaluates the 3IM in a more objective framework while also incorporating recent advances in QLCS theory, including the importance of low-level LP shear for mesovortex formation. Motivated by the recent findings of Brown et al. (2024), this study explored the potential of using upstream LP01 and LN03 shear relative to the leading line as predictors for mesovortex tornadoes. A novel leading-line analysis technique was created to isolate the leading line of QLCSs in both WoFS forecasts and MRMS observations to calculate system-relative LP01 and LN03 shear (Fig. 5). These shear components were combined with local tortuosity, a measure of local-line curvature, to produce a new composite parameter for QLCS tornado prediction, QTor [Eq. (6)]. This study serves as an initial proof of concept for system-relative, probabilistic mesovortex tornado prediction using a convection-allowing ensemble.

To subjectively evaluate QTor's performance, forecasts from four QLCS case studies were analyzed, which differed in location, environment, and season (Fig. 2). The results from each case study are summarized as follows:

- 15 December 2021 cold-season derecho: This case featured a broad area of enhanced QTor and high exceedance probabilities that fully encompassed all tornado reports (Fig. 7). Though exceedance probabilities decreased with increasing forecast time, QTor still predicted regions most conducive for tornado formation with high confidence over 5 h in advance. Leading-line extent errors contributed to a false alarm region along the southern portion of the QLCS, but this signal dissipates in space and time, unlike the broader, persistent signal in the northern swath.
- 30 March 2022 Southeast U.S. QLCS: QTor forecasts exhibited smaller areas of enhancement due to strong LP01 shear and weak LN03 shear (Figs. 10 and 11). Nonetheless, most tornado reports were collocated with local maxima in QTor 75th percentile and probability of exceeding 2.5 (Fig. 11). False alarm areas were primarily linked to cell mergers with the leading line.

Brought to you by NOAA Library | Unauthenticated | Downloaded 09/14/26 03:13 PM UTC

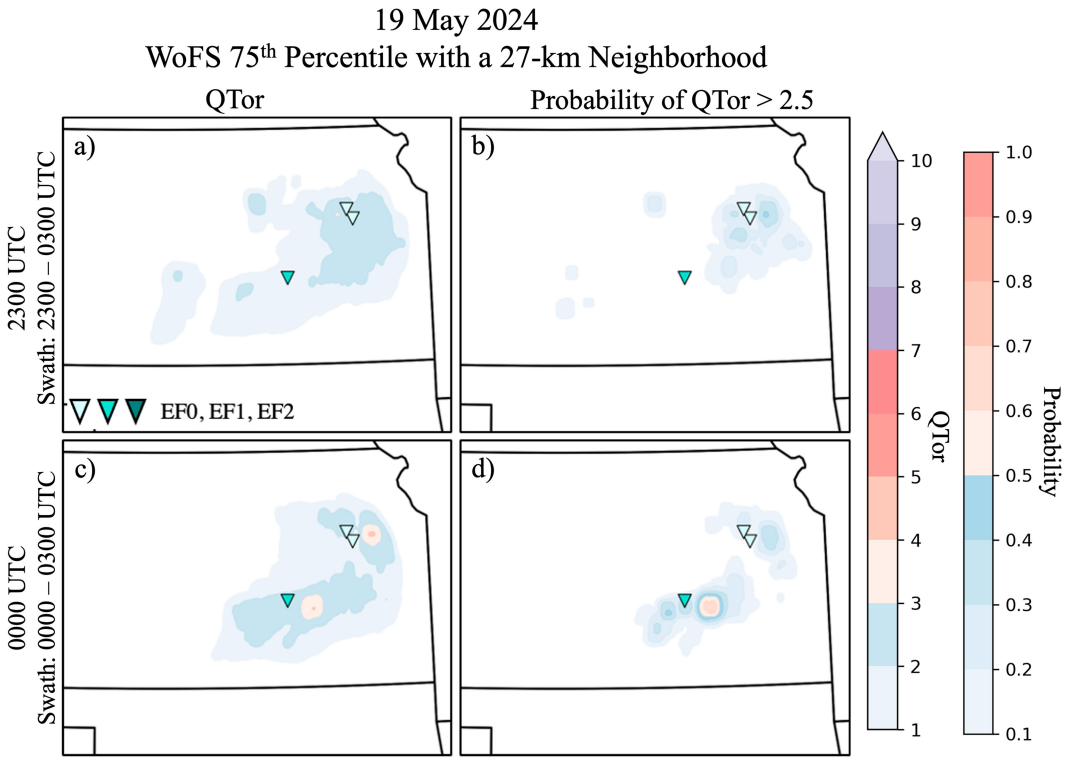


FIG. 19. As in Fig. 7, but for the 19 May 2024 QLCS.

- 12 May 2022 warm-season derecho: QTor forecasts highlighted the region most favorable for mesovortex tornadoes, aligning well with documented tornado reports and providing lead times exceeding 3 h in some forecasts (Fig. 14).
- 19 May 2024 null case: In this null case, QTor values and exceedance probabilities remained low during the QLCS's 2-h nontornadic phase and increased only in localized areas near the reported tornadoes (Fig. 19).

These results demonstrate QTor's potential to identify tornadic segments of QLCSs with substantial lead time, but several limitations currently hinder its broader utility. First, the dataset of cases is small and relies on subjective verification, limiting the generalizability of results across all QLCS environments. Additionally, QTor forecast accuracy is sensitive to WoFS errors in line orientation, extent, and storm mode, each of which impact shear and tortuosity calculations and can degrade performance. Limitations in the QLCS object and leading-line identification algorithms also contribute to false alarms, particularly in cases involving trailing cellular convection or merging cells. Moreover, calculations of SM are currently manually estimated, and automating this step will be crucial for real-time, operational applicability.

To address these limitations, several key avenues for future work are proposed. First, QTor will be applied to a broader and more diverse set of observed QLCS cases spanning different regions, environments, and seasons. Objective verification techniques and bulk performance metrics will be used to rigorously evaluate QTor's skill. Expanding the case database will also help clarify how to interpret QTor's numerical values. For example, while a QTor value of eight may indicate a more favorable environment for mesovortex tornadoes than a value of five, but the precise implications of such differences remain uncertain given the current subset of cases.

Machine learning techniques will be explored to optimize the QTor equation, tune thresholds, and explore the possibility of using region-specific shear criteria. QTor will also be compared to explicit measures of mesovortex potential, such as 0–2-km vertical vorticity and updraft helicity from WoFS forecasts. These fields may eventually be incorporated into a refined QTor equation. Additionally, sensitivity analysis and tuning of the object identification algorithm will be conducted to reduce errors associated with trailing cellular convection and storm mergers.

QTor has the potential to function as both a diagnostic tool, when applied to observations and a state analysis, and as a predictive tool when implemented into convection-allowing models, ensembles, and real-time analysis systems. However, several challenges must be addressed before operational implementation. The QTor algorithm must be fully automated and adapted for seamless integration into WoFS and other NWP systems. The incorporation of machine learning approaches may further enhance QTor by integrating its components, along with other predictors relevant to mesovortex tornadogenesis, to improve efficiency and forecast skill. Ultimately, a finalized, automated QTor prototype will be tested in an operational environment such as the NOAA Hazardous Weather

Brought to you by NOAA Library | Unauthenticated | Downloaded 09/14/26 03:13 PM UTC

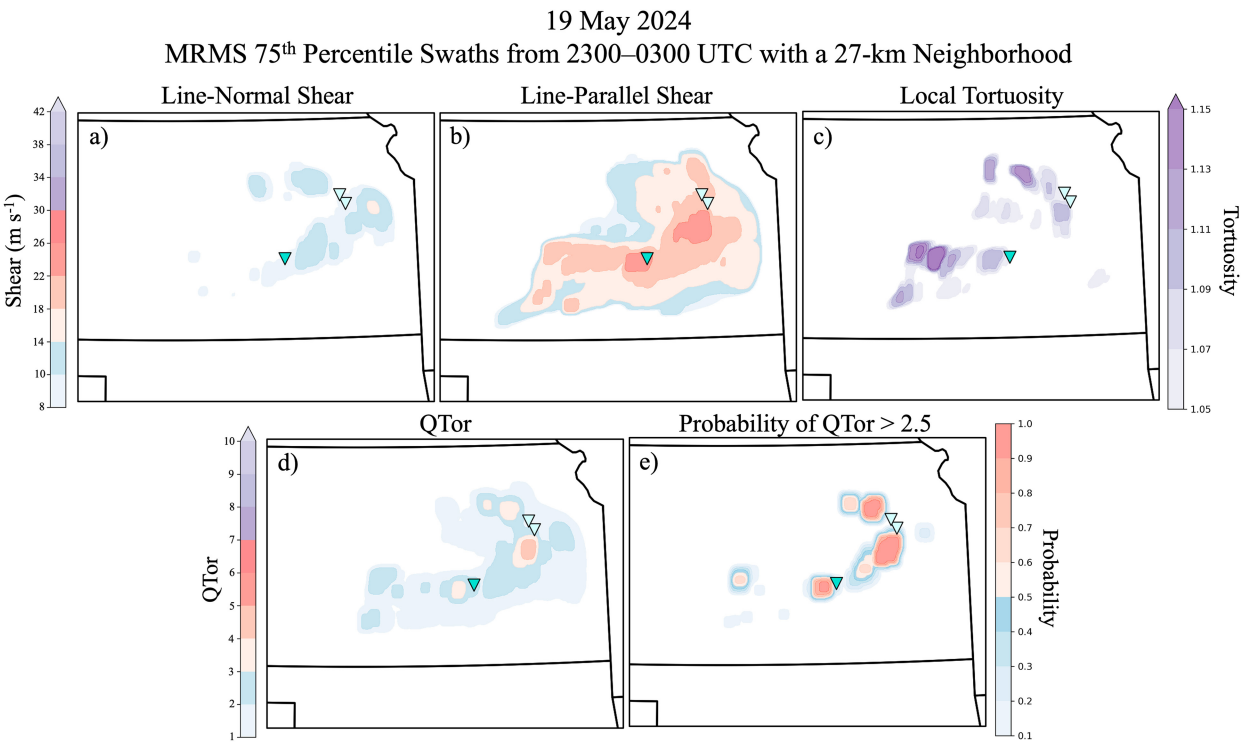


FIG. 20. As in Fig. 8, but for the 19 May 2024 QLCS.

Testbed (HWT; Clark et al. 2020, 2021) to assess real-time performance and gather forecaster feedback that will guide future refinements.

Acknowledgments. Funding for this research was provided by NOAA/Office of Oceanic and Atmospheric Research under NOAA–University of Oklahoma Cooperative Agreement NA21OAR4320204, U.S. Department of Commerce, and the Warn-on-Forecast project. M. C. Brown was additionally supported by NSF AGS-2414969, through the NSF AGS-PRF program. The authors would like to extend their gratitude to Dr. Mike Coniglio for his valuable feedback, which greatly helped improve this manuscript and our approach to reducing QTor false alarms. The authors also thank the four anonymous reviewers for their thoughtful suggestions. All analyses and visualizations were produced using the open-sourced Anaconda Python distribution (v.3.6) and the SciPy (Virtanen et al. 2020), Matplotlib (Hunter 2007), Shapely (Gillies et al. 2023), netCDF4 (Unidata 2019), NumPy (Harris et al. 2020), scikit-image (van der Walt et al. 2014), Cartopy (Met Office 2010–2015), Jupyter (Kluyver et al. 2016), and scikit-learn (Pedregosa et al. 2011) packages.

Data availability statement. All datasets and software used for this study are stored on the NSSL high-performance computing server, and the data are available upon request. Processing software for object tracking and matching is hosted at https://github.com/WarnOnForecast/MontePython.

APPENDIX

QTor Sensitivity Experiments

Sensitivity experiments were conducted to better understand QTor's behavior under varying environmental and geometric conditions. The first experiment examines how LP01 shear, LN03 shear, and QTor respond to variations in leading-line orientation relative to a uniform shear field (orientation of 45°) and a fixed shear vector (Fig. A1). For simplicity, we assume no curvature of the leading line (i.e., tortuosity is one).

QTor reaches a minimum of zero whenever the LN03 shear is negative, meaning the LN03 shear vector points into the storm. In these cases, developing mesovortices are quickly shed rearward, reducing the potential for tornadogenesis. This behavior is also consistent with outflow-dominant QLCS segments, such as those described in the 3IM (Fig. 1; Schaumann and Przybylinksi 2012) framework and RKW theory (Rotunno et al. 1988). In contrast, QTor is maximized when both LP01 and LN03 components are present, reflecting the combined influence of RKW theory and the findings of Brown et al. (2024). QTor reaches a secondary minimum when the leading line is either fully parallel or orthogonal to the shear vector. When the leading line and shear vector are aligned (e.g., both are 45°), all the shear is LP, leaving zero LN03 shear. Conversely, when the line is oriented 90° from the shear vector (e.g., 135° in this case; Fig. A1), all shear is LN, so LP01 is zero.

Brought to you by NOAA Library | Unauthenticated | Downloaded 09/14/26 03:13 PM UTC

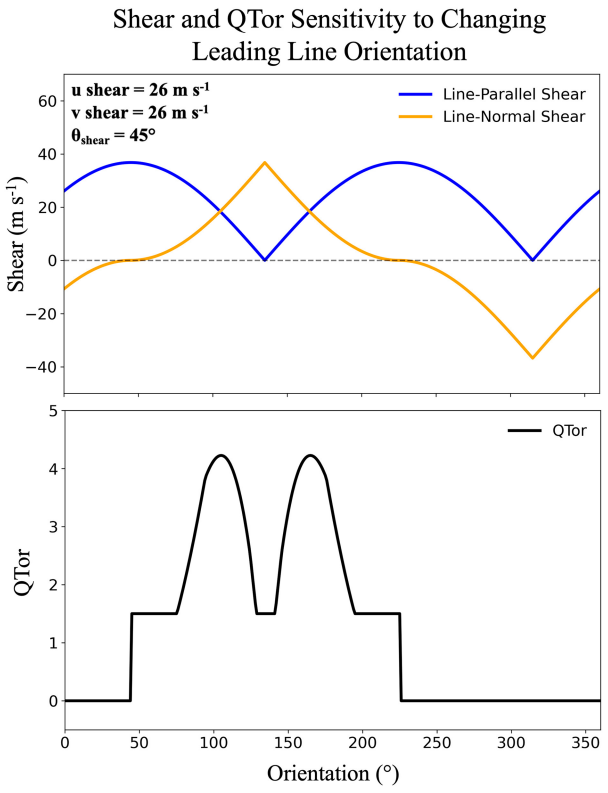


FIG. A1. (top) Sensitivity of LP01 and LN03 shear and (bottom) QTor to changes in leading-line orientation, assuming a constant shear field, constant shear angle (θ_{shear}), and no curvature. This pattern has a periodicity of π.

These trends hold across different shear vector orientations (not shown). However, the precise orientation angles at which QTor minima and maxima occur shift depending on the background shear direction. Additionally, QTor amplitude is sensitive to the environmental shear magnitude, with stronger shear yielding higher QTor.

The second sensitivity experiment examines how QTor responds to bowing segments within an idealized QLCS embedded in a uniform flow field (Fig. A2). In a southerly flow regime, QTor is zero on the southern side of the bow apex, where the shear points into/behind the storm. QTor is maximized on the northern side of the bow apex due to the increased curvature, with values ranging between 3 and 4 (Fig. A2a). QTor reaches a secondary minimum anywhere along the straight portions of the leading line. A similar pattern occurs in a northerly flow regime, except the QTor maximum shifts to the southern side of the bow apex, while QTor drops to zero on the northern side (Fig. A2b).

Under purely westerly flow, QTor is minimized along the straight portions of the line but maximized on both sides of the bowing apex (Fig. A2c). In contrast, easterly flow yields zero QTor everywhere along the leading line as the shear vector points into the storm. More generally, whenever the shear has a negative u component (i.e., an easterly component), QTor is zero everywhere along the leading line (Fig. A2d).

Similar to the southerly flow regime (Fig. A2a), QTor is maximized north of the bow apex in southwesterly flow (Fig. A2e). However, QTor along the southern side of the bow apex is no longer zero as the shear vector points away from the storm. The QTor values are also higher (3–4) along the straight portions of the leading line compared to the southerly example because both the LP and LN components contribute (consistent with Fig. A1). Similar differences are present between the northerly and northwesterly flows (Figs. A2b,f). With northwesterly winds, QTor is maximized along the southern edge of the bow echo, and QTor is nonzero along the northern edge (Fig. A2f). The values of QTor along the straight portions of the leading line are also higher in the northwesterly flow than compared to when the flow is purely northerly.

Overall, this experiment highlights how bowing segments increase QTor through the combined effects of increased curvature [via the tortuosity multiplier in Eq. (6)] and variations in local leading-line orientation relative to the ambient shear vector.

The next two experiments assess the impact of various shear (Fig. A3) and tortuosity thresholds (Fig. A4) on QTor calculations [Eq. (6)]. Only results from the 30 March 2022 case are shown, as it exhibited the most sensitivity to these changes.

Initially, LP01 and LN03 shear thresholds were set to 7 and 15 m s^{-1}, respectively (Figs. A3a,b). The LN03 threshold aligned the 3IM threshold (Fig. 1), while 7 m s^{-1} was chosen based on findings from Brown et al. (2024), where cyclonic mesovortices were more prevalent above this threshold. However, using an LN03 threshold of 15 m s^{-1} resulted in QTor values being overly dependent on LP01 shear. Alternative thresholds were tested to determine the most effective combination for the three cases examined. For 30 March 2022, setting LP01 and LN03 thresholds to 8 and 10 m s^{-1}, respectively, increased QTor values near the TN tornadoes and in the southern swath from southeast MS to central AL (Figs. A3c,d). Conversely, increasing both thresholds to 10 and 15 m s^{-1} resulted in lower QTor values (Figs. A3e,f). When the LN03 shear threshold was reduced to match the LP01 threshold of 10 m s^{-1} (Figs. A3g,h), results were similar to the 8 and 10 m s^{-1} experiment (Figs. A3c,d) but with lower QTor values around the TN tornadoes and in southern MS (Figs. A3g,h). Overall, the 8 and 10 m s^{-1} thresholds were selected, as they provided the best discrimination of QTor values near reported tornadoes, a more continuous QTor field between 2.0 and 4.0, and better representation for all case studies (not shown).

The next experiment examines QTor's sensitivity to different tortuosity thresholds and methods (Fig. A4). Initially, the local tortuosity term was normalized by 1.03, which was roughly the 50th–75th percentile of tortuosity depending on the case study, and multiplied with the LP01 and LN03 terms [Eq. (6)]. However, since tortuosity values are small compared to LP01 and LN03 terms, its effect on QTor was minimal (Figs. A4a,b vs Figs. A4c,d). Doubling tortuosity

Brought to you by NOAA Library | Unauthenticated | Downloaded 09/14/26 03:13 PM UTC

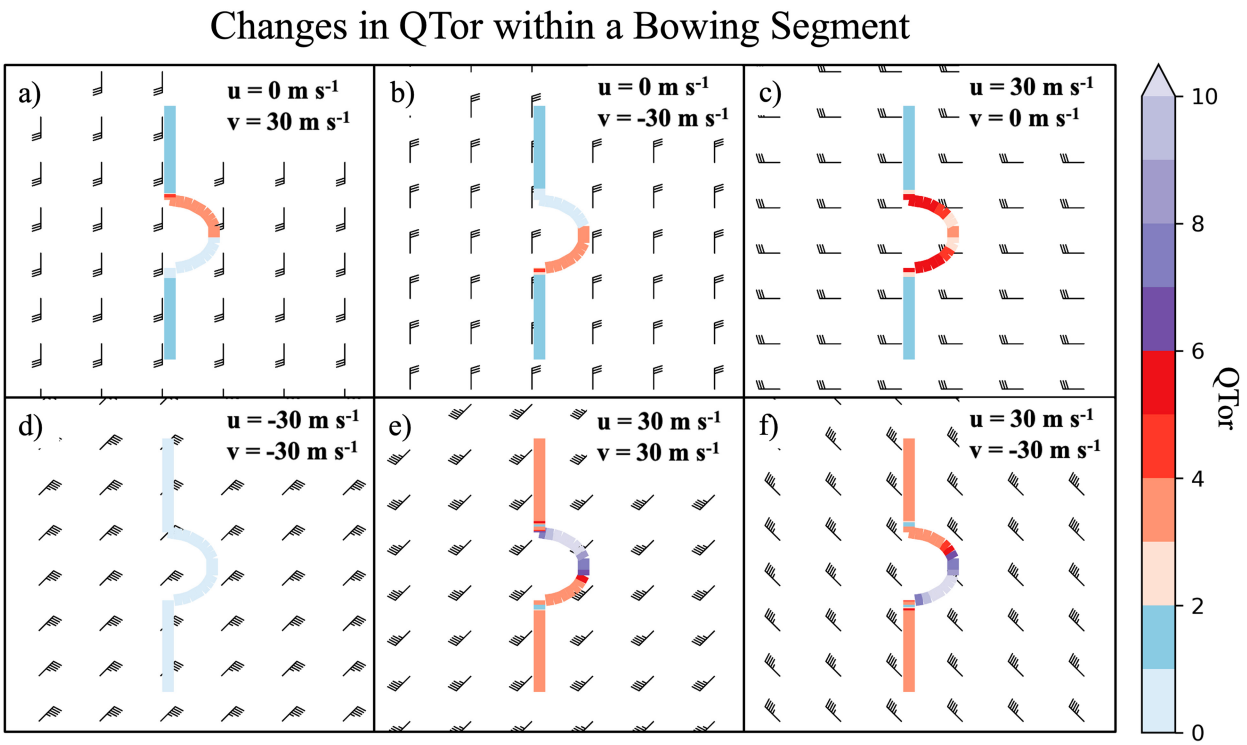


FIG. A2. Sensitivity of QTor in the presence of a bowing segment, assuming a straight north–south-oriented QLCS and a uniform flow field with (a) southerly, (b) northerly, (c) westerly, (d) northeasterly winds (this pattern is the same anytime the *u* component of shear is negative), (e) southwesterly, and (f) northwesterly.

(Figs. A4e,f) only inflated QTor values without adding any additional information. Consequently, a conditional tortuosity approach was adopted [Eq. (6)]. If local tortuosity exceeded 1.05, its term was set to 2, doubling QTor in high-curvature areas like bowing segments (Fig. A2). Otherwise, the term remained 1, leaving QTor unchanged. This method better identified tornado-prone areas, particularly from southeast MS to central AL (Figs. A4g,h), and was retained for the QTor equation's final version [Eq. (6)].

The final sensitivity experiment evaluates the effects of applying upper and lower bounds to the LP01 and LN03 shear components in the QTor equation [Eq. (6)]. An upper cap of 3.0 limits QTor to a maximum value of 18, assuming both shear components reach their cap and the tortuosity is 2 (Figs. A5a,b). This cap is especially useful in environments where one shear component dominates, such as the 30 March 2022 case (Fig. 10), by preventing that component from disproportionally influencing QTor and overshadowing contributions from the other terms. A lower cap of 0.5 was also applied to each shear component (Figs. A5c,d) to address cases where one shear term approaches zero. Although mesovortex tornado potential is reduced in such scenarios, a nonzero risk still exists. The lower cap ensures QTor does not drop to zero solely due to the absence of one shear component. Without these constraints, QTor values can become excessively large or zero (Figs. A5e,f), reducing interpretability. Thus, applying both upper and lower bounds helps to regulate QTor behaviors and maintain the parameter's relevance across a range of environmental conditions.

Brought to you by NOAA Library | Unauthenticated | Downloaded 09/14/26 03:13 PM UTC

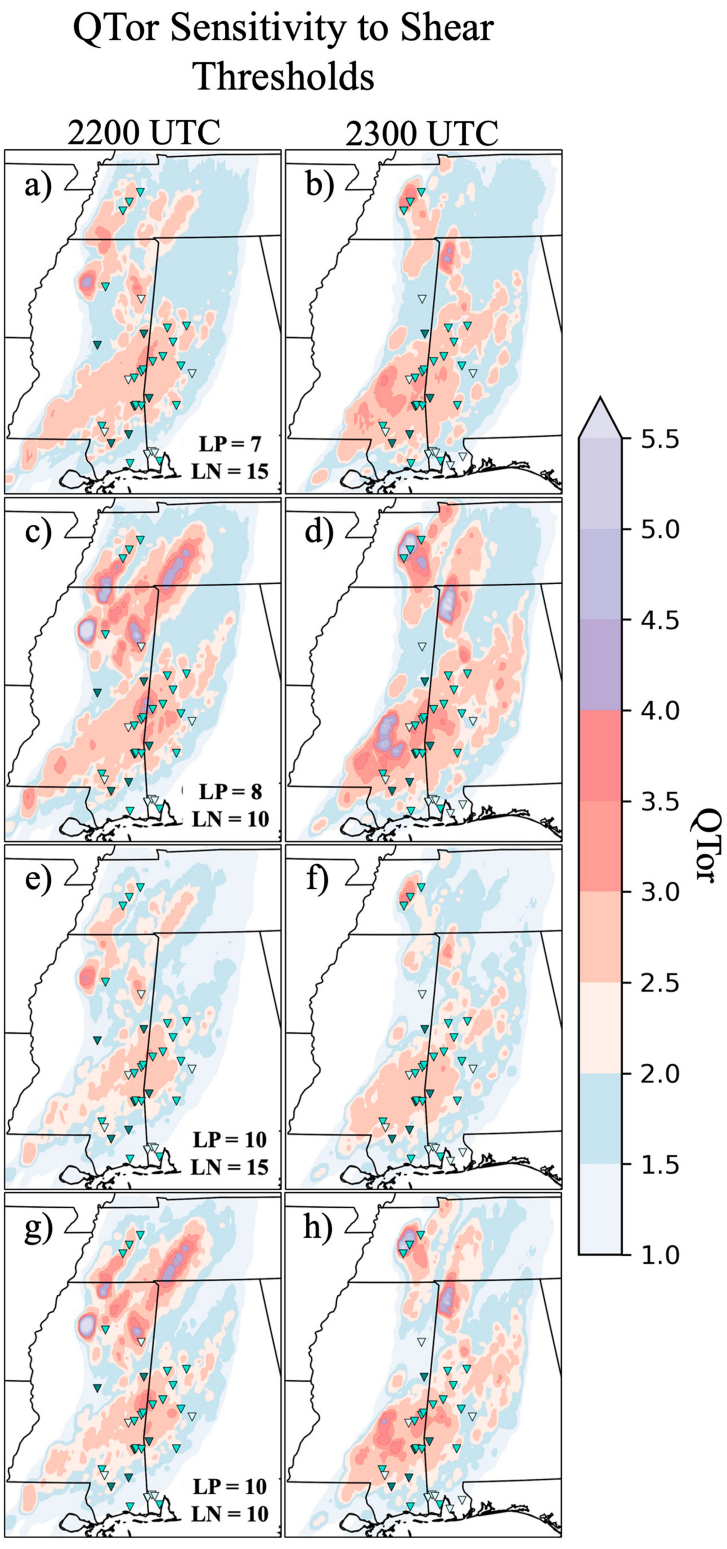


FIG. A3. Sensitivity of QTor [Eq. (6)] to changes in shear thresholds for the (left) 2200 UTC and (right) 2300 UTC forecasts from the 30 Mar 2022 QLCS case. The LP and LN thresholds, respectively, are (a),(b) 7 and 15, (c),(d) 8 and 10, (e),(f) 10 and 15, and (g),(h) 10 and 10 m s^{-1}. Note: Different QTor color bar intervals are used to better illustrate differences.

Brought to you by NOAA Library | Unauthenticated | Downloaded 09/14/26 03:13 PM UTC

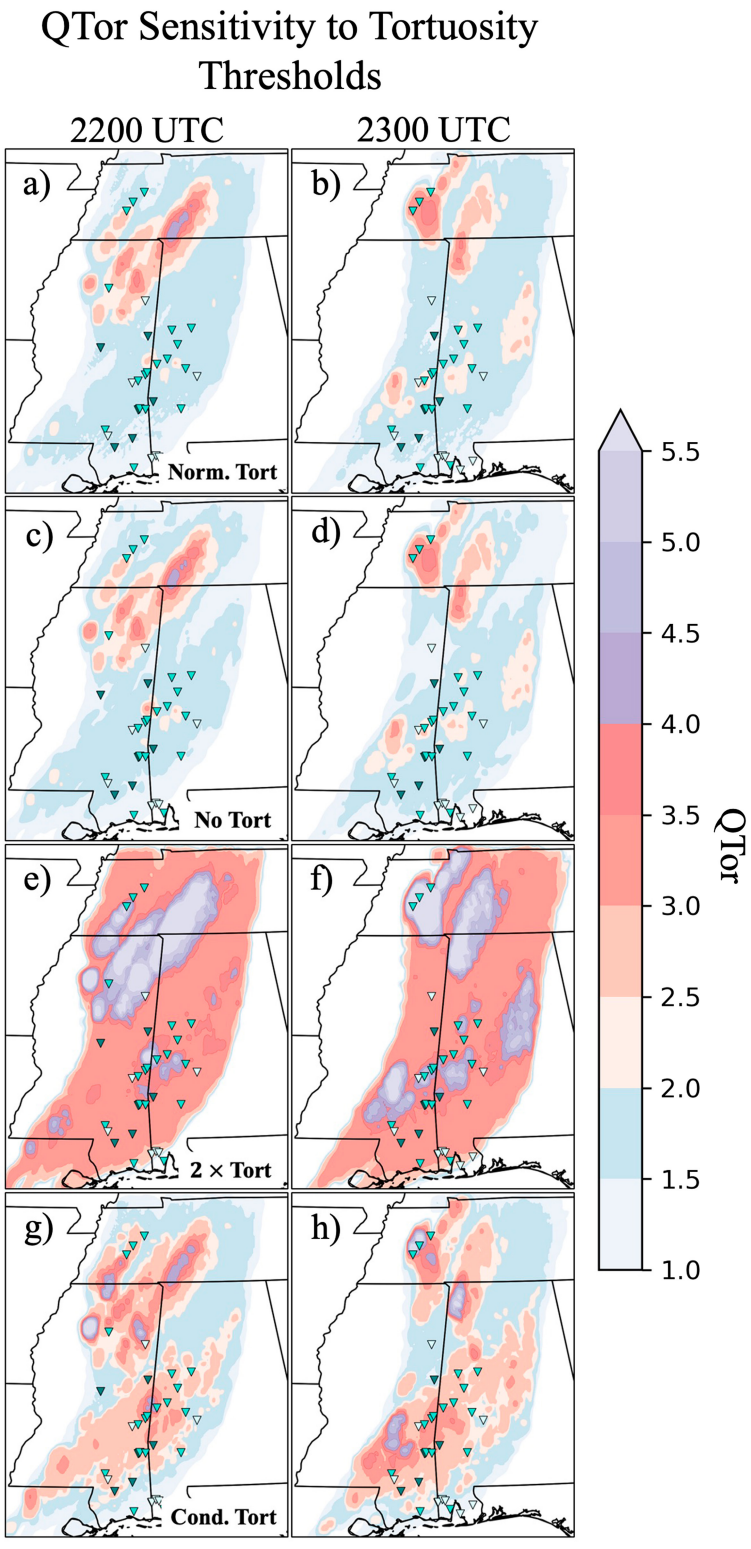


FIG. A4. As in Fig. A3, but for changes in tortuosity thresholds. (a),(b) The local tortuosity of each segment is normalized by 1.03 (approximately the 50th–75th percentile of tortuosity depending on the case), (c),(d) no tortuosity term, (e),(f) the local tortuosity of each segment is doubled, and (g),(h) a conditional tortuosity term is used as in Eq. (6).

Brought to you by NOAA Library | Unauthenticated | Downloaded 09/14/26 03:13 PM UTC

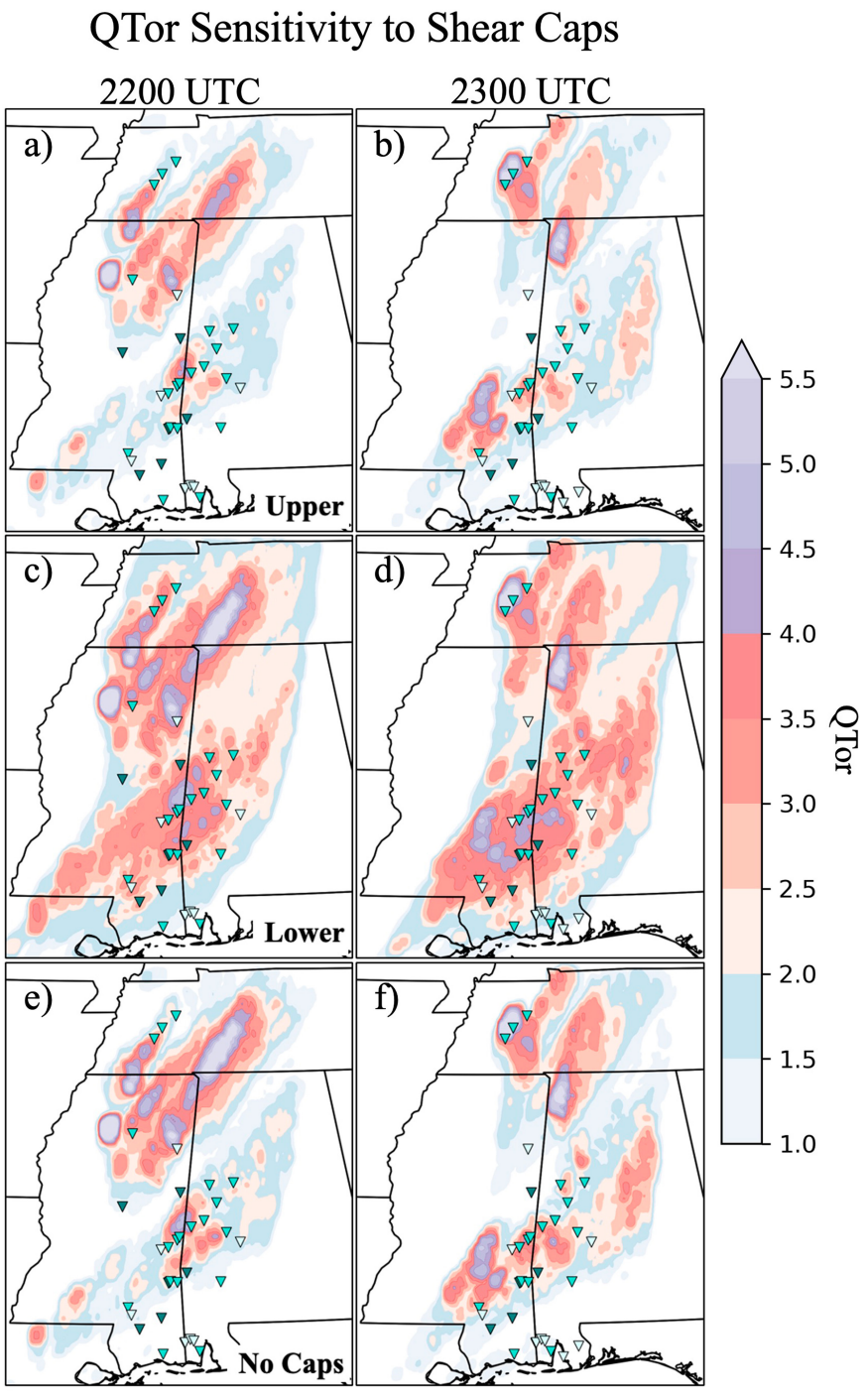


FIG. A5. Sensitivity of QTor to (a),(b) an upper cap of 3.0, (c),(d) a lower cap of 0.5, and (e),(f) no upper or lower cap for the (left) 2200 UTC and (right) 2300 UTC 30 Mar 2022 WoFS forecasts.

Brought to you by NOAA Library | Unauthenticated | Downloaded 09/14/26 03:13 PM UTC

REFERENCES

Ashley, W. S., A. J. Krmenec, and R. Schwantes, 2008: Vulnerability due to nocturnal tornadoes. *Wea. Forecasting*, **23**, 795–807, https://doi.org/10.1175/2008WAF2222132.1.

——, A. M. Haberlie, and J. Strohm, 2019: A climatology of quasi-linear convective systems and their hazards in the United States. *Wea. Forecasting*, **34**, 1605–1631, https://doi.org/10.1175/WAF-D-19-0014.1.

Atkins, N. T., J. M. Arnott, R. W. Przybylinski, R. A. Wolf, and B. D. Ketcham, 2004: Vortex structure and evolution within bow echoes. Part I: Single-Doppler and damage analysis of the 29 June 1998 derecho. *Mon. Wea. Rev.*, **132**, 2224–2242, https://doi.org/10.1175/1520-0493(2004)132<2224:VSAEWB>2.0.CO;2.

——, C. S. Bouchard, R. W. Przybylinski, R. J. Trapp, and G. Schmocker, 2005: Damaging surface wind mechanisms within the 10 June 2003 Saint Louis bow echo during BAMEX. *Mon. Wea. Rev.*, **133**, 2275–2296, https://doi.org/10.1175/MWR2973.1.

Britt, K. C., P. S. Skinner, P. L. Heinselman, and K. H. Knopfmeier, 2020: Effects of horizontal grid spacing and inflow environment on forecasts of cyclic mesocyclogenesis in NSSL's Warn-on-Forecast System (WoFS). *Wea. Forecasting*, **35**, 2423–2444, https://doi.org/10.1175/WAF-D-20-0094.1.

——, ——, ——, C. K. Potvin, M. L. Flora, B. Matilla, K. H. Knopfmeier, and A. E. Reinhart, 2024: Verification of quasi-linear convective systems predicted by the Warn-on-Forecast System (WoFS). *Wea. Forecasting*, **39**, 155–176, https://doi.org/10.1175/WAF-D-23-0106.1.

Brotzge, J. A., S. E. Nelson, R. L. Thompson, and B. T. Smith, 2013: Tornado probability of detection and lead time as a function of convective mode and environmental parameters. *Wea. Forecasting*, **28**, 1261–1276, https://doi.org/10.1175/WAF-D-12-00119.1.

Brown, M. C., G. R. Marion, and M. C. Coniglio, 2024: Influence of low-level shear orientation and magnitude on the evolution and rotation of idealized squall lines. Part I: Storm morphology and bulk updraft/mesovortex attributes. *Mon. Wea. Rev.*, **152**, 2089–2110, https://doi.org/10.1175/MWR-D-23-0262.1.

——, ——, and ——, 2026: Influence of low-level shear orientation and magnitude on the evolution and rotation of idealized squall lines. Part II: Storm propagation and dynamic feedbacks. *Mon. Wea. Rev.*, **154**, 203–225, https://doi.org/10.1175/MWR-D-25-0240.1.

Chasteen, M. B., and S. E. Koch, 2022: Multiscale aspects of the 26–27 April 2011 tornado outbreak. Part I: Outbreak chronology and environmental evolution. *Mon. Wea. Rev.*, **150**, 309–335, https://doi.org/10.1175/MWR-D-21-0013.1.

Ciuricä, S., and Coauthors, 2019: Arterial tortuosity. *Hypertension*, **73**, 951–960, https://doi.org/10.1161/HYPERTENSIONAHA.118.11647.

Clark, A. J., and Coauthors, 2020: A real-time, simulated forecasting experiment for advancing the prediction of hazardous convective weather. *Bull. Amer. Meteor. Soc.*, **101**, E2022–E2024, https://doi.org/10.1175/BAMS-D-19-0298.1.

——, and Coauthors, 2021: A real-time, virtual spring forecasting experiment to advance severe weather prediction. *Bull. Amer. Meteor. Soc.*, **102**, E814–E816, https://doi.org/10.1175/BAMS-D-20-0268.1.

Coffer, B. E., M. D. Parker, J. M. L. Dahl, L. J. Wicker, and A. J. Clark, 2017: Volatility of tornadogenesis: An ensemble of simulated nontornadic and tornadic supercells in VORTEX2 environments. *Mon. Wea. Rev.*, **145**, 4605–4625, https://doi.org/10.1175/MWR-D-17-0152.1.

Davis, J. M., and M. D. Parker, 2014: Radar climatology of tornadic and nontornadic vortices in high-shear, low-CAPE environments in the mid-Atlantic and southeastern United States. *Wea. Forecasting*, **29**, 828–853, https://doi.org/10.1175/WAF-D-13-00127.1.

Dowell, D. C., and Coauthors, 2022: The High-Resolution Rapid Refresh (HRRR): An hourly updating convection-allowing forecast model. Part I: Motivation and system description. *Wea. Forecasting*, **37**, 1371–1395, https://doi.org/10.1175/WAF-D-21-0151.1.

Dudhia, J., 1989: Numerical study of convection observed during the winter monsoon experiment using a mesoscale two-dimensional model. *J. Atmos. Sci.*, **46**, 3077–3107, https://doi.org/10.1175/1520-0469(1989)046<3077:NSOCOD>2.0.CO;2.

Flora, M. L., P. S. Skinner, C. K. Potvin, A. E. Reinhart, T. A. Jones, N. Yussouf, and K. H. Knopfmeier, 2019: Object-based verification of short-term, storm-scale probabilistic mesocyclone guidance from an experimental Warn-on-Forecast System. *Wea. Forecasting*, **34**, 1721–1739, https://doi.org/10.1175/WAF-D-19-0094.1.

Flournoy, M. D., and M. C. Coniglio, 2019: Origins of vorticity in a simulated tornadic mesovortex observed during PECAN on 6 July 2015. *Mon. Wea. Rev.*, **147**, 107–134, https://doi.org/10.1175/MWR-D-18-0221.1.

——, ——, E. N. Rasmussen, J. C. Furtado, and B. E. Coffer, 2020: Modes of storm-scale variability and tornado potential in VORTEX2 near- and far-field tornadic environments. *Mon. Wea. Rev.*, **148**, 4185–4207, https://doi.org/10.1175/MWR-D-20-0147.1.

Funk, T. W., K. E. Darmofal, J. D. Kirkpatrick, V. L. DeWald, R. W. Przybylinski, G. K. Schmocker, and Y. J. Lin, 1999: Storm reflectivity and mesocyclone evolution associated with the 15 April 1994 squall line over Kentucky and southern Indiana. *Wea. Forecasting*, **14**, 976–993, https://doi.org/10.1175/1520-0434(1999)014<0976:SRAMEA>2.0.CO;2.

Galarneau, T. J., Jr., L. J. Wicker, K. H. Knopfmeier, W. J. S. Miller, P. S. Skinner, and K. A. Wilson, 2022: Short-term prediction of a nocturnal significant tornado outbreak using a convection-allowing ensemble. *Wea. Forecasting*, **37**, 1027–1047, https://doi.org/10.1175/WAF-D-21-0160.1.

Gibbs, J. G., 2021: Evaluating precursor signals for QLCS tornado and higher impact straight-line wind events. *J. Oper. Meteor.*, **9**, 62–75, https://doi.org/10.15191/nwajom.2021.0905.

Gillies, S., and Coauthors, 2023: Shapely (2.1.2). Zenodo, https://doi.org/10.5281/zenodo.5597138.

Harris, C. R., and Coauthors, 2020: Array programming with NumPy. *Nature*, **585**, 357–362, https://doi.org/10.1038/s41586-020-2649-2.

Heinselman, P. L., and Coauthors, 2024: Warn-on-Forecast System: From vision to reality. *Wea. Forecasting*, **39**, 75–95, https://doi.org/10.1175/WAF-D-23-0147.1.

Hill, C., C. DeLuca, B. M. Suarez, and A. Da Silva, 2004: The architecture of the Earth system modeling framework. *Comput. Sci. Eng.*, **6**, 18–28, https://doi.org/10.1109/MCISE.2004.1255817.

Hong, S.-Y., Y. Noh, and J. Dudhia, 2006: A new vertical diffusion package with an explicit treatment of entrainment processes. *Mon. Wea. Rev.*, **134**, 2318–2341, https://doi.org/10.1175/MWR3199.1.

Brought to you by NOAA Library | Unauthenticated | Downloaded 09/14/26 03:13 PM UTC

Houtekamer, P. L., and F. Zhang, 2016: Review of the ensemble Kalman filter for atmospheric data assimilation. *Mon. Wea. Rev.*, **144**, 4489–4532, https://doi.org/10.1175/MWR-D-15-0440.1.

Houze, R. A., Jr., 2018: 100 years of research on mesoscale convective systems. *A Century of Progress in Atmospheric and Related Sciences: Celebrating the American Meteorological Society Centennial*, *Meteor. Monogr.*, No. **59**, Amer. Meteor. Soc., https://doi.org/10.1175/AMSMONOGRAPHS-D-18-0001.1.

Hu, M., H. Shao, D. Stark, K. Newman, C. Zhou, and X. Zhang, 2016: Gridpoint Statistical Interpolation (GSI) user's guide version 3.5. Developmental Testbed Center Rep., 148 pp., https://dtcenter.org/com-GSI/users/docs/users_guide/GSIUserGuide_v3.5.pdf.

Hunter, J. D., 2007: Matplotlib: A 2D graphics environment. *Comput. Sci. Eng.*, **9**, 90–95, https://doi.org/10.1109/MCSE.2007.55.

Iacono, M. J., J. S. Delamere, E. J. Mlawer, M. W. Shephard, S. A. Clough, and W. D. Collins, 2008: Radiative forcing by long-lived greenhouse gases: Calculations with the AER radiative transfer models. *J. Geophys. Res.*, **113**, D13103, https://doi.org/10.1029/2008JD009944.

James, J. J. J., C. Ling, C. D. Karstens, J. Correia Jr., K. Calhoun, T. Meyer, and D. LaDue, 2020: Forecasters' cognitive task analysis and mental workload analysis of issuing Probabilistic Hazard Information (PHI) during FACETs PHI prototype experiment. *Wea. Forecasting*, **35**, 1505–1521, https://doi.org/10.1175/WAF-D-19-0194.1.

Johns, R. H., and W. D. Hirt, 1987: Derechos: Widespread convectively induced windstorms. *Wea. Forecasting*, **2**, 32–49, https://doi.org/10.1175/1520-0434(1987)002<0032:dwciw>2.0.co;2.

Jones, T. A., D. Stensrud, L. Wicker, P. Minnis, and R. Palikonda, 2015: Simultaneous radar and satellite data storm-scale assimilation using an ensemble Kalman filter approach for 24 May 2011. *Mon. Wea. Rev.*, **143**, 165–194, https://doi.org/10.1175/MWR-D-14-00180.1.

——, K. Knopfmeier, D. Wheatley, G. Creager, P. Minnis, and R. Palikonda, 2016: Storm-scale data assimilation and ensemble forecasting with the NSSL experimental Warn-on-Forecast system. Part II: Combined radar and satellite data experiments. *Wea. Forecasting*, **31**, 297–327, https://doi.org/10.1175/WAF-D-15-0107.1.

——, X. Wang, P. Skinner, A. Johnson, and Y. Wang, 2018: Assimilation of *GOES-13* imager clear-sky water vapor (6.5 μm) radiances into a Warn-on-Forecast system. *Mon. Wea. Rev.*, **146**, 1077–1107, https://doi.org/10.1175/MWR-D-17-0280.1.

——, P. Skinner, N. Yussouf, K. Knopfmeier, A. Reinhart, and D. Dowell, 2019: Forecasting high-impact weather in landfalling tropical cyclones using a Warn-on-Forecast system. *Bull. Amer. Meteor. Soc.*, **100**, 1405–1417, https://doi.org/10.1175/BAMS-D-18-0203.1.

——, and Coauthors, 2020: Assimilation of *GOES-16* radiances and retrievals into the Warn-on-Forecast System. *Mon. Wea. Rev.*, **148**, 1829–1859, https://doi.org/10.1175/MWR-D-19-0379.1.

Karstens, C. D., and Coauthors, 2018: Development of a human–machine mix for forecasting severe convective events. *Wea. Forecasting*, **33**, 715–737, https://doi.org/10.1175/WAF-D-17-0188.1.

Kerr, C. A., and F. Alsheimer, 2022: Storm-scale predictability and analysis of the 13 April 2020 Central Savannah River Area tornado outbreak. *Wea. Forecasting*, **37**, 901–913, https://doi.org/10.1175/WAF-D-21-0185.1.

King, J. R., M. D. Parker, K. D. Sherburn, and G. M. Lackmann, 2017: Rapid evolution of cool season, low-CAPE severe thunderstorm environments. *Wea. Forecasting*, **32**, 763–779, https://doi.org/10.1175/WAF-D-16-0141.1.

Kleist, D. T., D. F. Parrish, J. C. Derber, R. Treadon, W.-S. Wu, and S. Lord, 2009: Introduction of the GSI into the NCEP Global Data Assimilation System. *Wea. Forecasting*, **24**, 1691–1705, https://doi.org/10.1175/2009WAF2222201.1.

Kluyver, T., and Coauthors, 2016: Jupyter notebooks—A publishing format for reproducible computational workflows. *Positioning and Power in Academic Publishing: Players, Agents and Agendas*, F. Loizides and B. Schmidt, Eds., IOS Press, 87–90.

Lawson, J. R., J. S. Kain, N. Yussouf, D. C. Dowell, D. M. Wheatley, K. H. Knopfmeier, and T. A. Jones, 2018: Advancing from convection-allowing NWP to Warn-on-Forecast: Evidence of progress. *Wea. Forecasting*, **33**, 599–607, https://doi.org/10.1175/WAF-D-17-0145.1.

Lee, B. D., and R. B. Wilhelmson, 1997: The numerical simulation of non-supercell tornadogenesis. Part I: Initiation and evolution of pretornadic misocyclone circulations along a dry outflow boundary. *J. Atmos. Sci.*, **54**, 32–60, https://doi.org/10.1175/1520-0469(1997)054<0032:TNSONS>2.0.CO;2.

——, and ——, 2000: The numerical simulation of nonsupercell tornadogenesis. Part III: Parameter tests investigating the role of CAPE, vortex sheet strength, and boundary layer vertical shear. *J. Atmos. Sci.*, **57**, 2246–2261, https://doi.org/10.1175/1520-0469(2000)057<2246:TNSONT>2.0.CO;2.

Lyza, A. W., A. W. Clayton, K. R. Knupp, E. Lenning, M. T. Friedlein, R. L. Castro, and E. S. Bentley, 2017: Analysis of mesovortex characteristics, behavior, and interactions during the second 30 June–1 July 2014 midwestern derecho event. *Electron. J. Severe Storms Meteor.*, **12** (2), https://doi.org/10.55599/ejssm.v12i2.67.

Mahale, V. N., J. A. Brotzge, and H. B. Bluestein, 2012: An analysis of vortices embedded within a quasi-linear convective system using X-band polarimetric radar. *Wea. Forecasting*, **27**, 1520–1537, https://doi.org/10.1175/WAF-D-11-00135.1.

Mansell, E. R., C. L. Ziegler, and E. C. Bruning, 2010: Simulated electrification of a small thunderstorm with two-moment bulk microphysics. *J. Atmos. Sci.*, **67**, 171–194, https://doi.org/10.1175/2009JAS2965.1.

Marion, G. R., and R. J. Trapp, 2021: Controls of quasi-linear convective system tornado intensity. *J. Atmos. Sci.*, **78**, 1189–1205, https://doi.org/10.1175/JAS-D-20-0164.1.

Markowski, P., and Y. Richardson, 2010: *Mesoscale Meteorology in Midlatitudes.* Wiley-Blackwell, 431 pp.

Martin, J. J., and Coauthors, 2024: Cb-WoFS: Migrating the Warn-on-Forecast System to the cloud. *Bull. Amer. Meteor. Soc.*, **105**, E1962–E1971, https://doi.org/10.1175/BAMS-D-23-0296.1.

Mellor, G. L., and T. Yamada, 1982: Development of a turbulence closure model for geophysical fluid problems. *Rev. Geophys.*, **20**, 851–875, https://doi.org/10.1029/RG020i004p00851.

Met Office, 2010–2015: Cartopy: A cartographic Python library with a Matplotlib interface. https://scitools.org.uk/cartopy.

Nakanishi, M., and H. Niino, 2004: An improved Mellor–Yamada level-3 model with condensation physics: Its design and verification. *Bound.-Layer Meteor.*, **112**, 1–31, https://doi.org/10.1023/B:BOUN.0000020164.04146.98.

Brought to you by NOAA Library | Unauthenticated | Downloaded 09/14/26 03:13 PM UTC

Newman, J. F., and P. L. Heinselman, 2012: Evolution of a quasi-linear convective system sampled by phased array radar. *Mon. Wea. Rev.*, **140**, 3467–3486, https://doi.org/10.1175/MWR-D-12-00003.1.

NOAA, 2024: Damage assessment toolkit. Accessed 20 June 2024, https://apps.dat.noaa.gov/stormdamage/damageviewer/.

NWS, 2023: QLCS tornado training. Accessed 18 August 2025, https://www.weather.gov/sgf/qlcs_tornado_training.

Orlanski, I., 1975: A rational subdivision of scales for atmospheric processes. *Bull. Amer. Meteor. Soc.*, **56**, 527–530.

Pardun, T. J., A. E. Reinhart, and M. C. Coniglio, 2025: A comparison between tornadic and nontornadic QLCS mesovortices using a multiradar analysis of operational and experimental MRMS products. *Wea. Forecasting*, **40**, 915–935, https://doi.org/10.1175/WAF-D-24-0050.1.

Parker, M. D., 2014: Composite VORTEX2 supercell environments from near-storm soundings. *Mon. Wea. Rev.*, **142**, 508–529, https://doi.org/10.1175/MWR-D-13-00167.1.

Pedregosa, F., and Coauthors, 2011: Scikit-learn: Machine learning in Python. *J. Mach. Learn. Res.*, **12**, 2825–2830.

Potvin, C. K., and Coauthors, 2022: An iterative storm segmentation and classification algorithm for convection-allowing models and gridded radar analyses. *J. Atmos. Oceanic Technol.*, **39**, 999–1013, https://doi.org/10.1175/JTECH-D-21-0141.1.

Przybylinski, R. W., 1995: The bow echo: Observations, numerical simulations, and severe weather detection methods. *Wea. Forecasting*, **10**, 203–218, https://doi.org/10.1175/1520-0434(1995)010<0203:TBEONS>2.0.CO;2.

Roberts, B., I. L. Jirak, A. J. Clark, S. J. Weiss, and J. S. Kain, 2019: PostProcessing and visualization techniques for convection-allowing ensembles. *Bull. Amer. Meteor. Soc.*, **100**, 1245–1258, https://doi.org/10.1175/BAMS-D-18-0041.1.

Rotunno, R., J. B. Klemp, and M. L. Weisman, 1988: A theory for strong, long-lived squall lines. *J. Atmos. Sci.*, **45**, 463–485, https://doi.org/10.1175/1520-0469(1988)045<0463:ATFSLL>2.0.CO;2.

Schaumann, J. S., and R. W. Przybylinksi, 2012: Operational application of 0-3 km bulk shear vectors in assessing quasi linear convective system mesovortex and tornado potential. *26th Conf. on Severe Local Storms*, Nashville, TN, Amer. Meteor. Soc., 142, https://ams.confex.com/ams/26SLS/webprogram/Paper212008.html.

Schwartz, C. S., and R. A. Sobash, 2017: Generating probabilistic forecasts from convection-allowing ensembles using neighborhood approaches: A review and recommendations. *Mon. Wea. Rev.*, **145**, 3397–3418, https://doi.org/10.1175/MWR-D-16-0400.1.

Sherburn, K. D., and M. D. Parker, 2014: Climatology and ingredients of significant severe convection in high-shear, low-CAPE environments. *Wea. Forecasting*, **29**, 854–877, https://doi.org/10.1175/WAF-D-13-00041.1.

——, ——, J. R. King, and G. M. Lackmann, 2016: Composite environments of severe and nonsevere high-shear, low-CAPE convective events. *Wea. Forecasting*, **31**, 1899–1927, https://doi.org/10.1175/WAF-D-16-0086.1.

Skinner, P. S., and Coauthors, 2018: Object-based verification of a prototype Warn-on-Forecast System. *Wea. Forecasting*, **33**, 1225–1250, https://doi.org/10.1175/WAF-D-18-0020.1.

——, and Coauthors, 2023: Interpreting Warn-on-Forecast System guidance, Part I: Review of probabilistic guidance concepts, product design, and best practices. *J. Oper. Meteor.*, **11**, 110–131, https://doi.org/10.15191/nwajom.2023.1109.

Skow, K. D., and C. Cogil, 2017: A high-resolution aerial survey and radar analysis of quasi-linear convective system surface vortex damage paths from 31 August 2014. *Wea. Forecasting*, **32**, 441–467, https://doi.org/10.1175/WAF-D-16-0136.1.

Smirnova, T. G., J. M. Brown, S. G. Benjamin, and J. S. Kenyon, 2016: Modifications to the Rapid Update Cycle land surface model (RUC LSM) available in the Weather Research and Forecasting (WRF) Model. *Mon. Wea. Rev.*, **144**, 1851–1865, https://doi.org/10.1175/MWR-D-15-0198.1.

Smith, B. T., R. L. Thompson, J. S. Grams, C. Broyles, and H. E. Brooks, 2012: Convective modes for significant severe thunderstorms in the contiguous United States. Part I: Storm classification and climatology. *Wea. Forecasting*, **27**, 1114–1135, https://doi.org/10.1175/WAF-D-11-00115.1.

Smith, T. M., and Coauthors, 2016: Multi-Radar Multi-Sensor (MRMS) severe weather and aviation products: Initial operating capabilities. *Bull. Amer. Meteor. Soc.*, **97**, 1617–1630, https://doi.org/10.1175/BAMS-D-14-00173.1.

SPC, 2023: Severe weather database. Accessed 20 June 2024, https://www.spc.noaa.gov/wcm/#data.

Squitieri, B. J., A. R. Wade, and I. L. Jirak, 2023a: A historical overview on the science of derechos: Part I: Identification, climatology, and societal impacts. *Bull. Amer. Meteor. Soc.*, **104**, E1709–E1733, https://doi.org/10.1175/BAMS-D-22-0217.1.

——, ——, and ——, 2023b: A historical overview on the science of derechos: Part II: Parent storm structure, environmental conditions, and history of numerical forecasts. *Bull. Amer. Meteor. Soc.*, **104**, E1734–E1763, https://doi.org/10.1175/BAMS-D-22-0278.1.

Stensrud, D. J., and Coauthors, 2009: Convective-scale warn-on-forecast system: A vision for 2020. *Bull. Amer. Meteor. Soc.*, **90**, 1487–1500, https://doi.org/10.1175/2009BAMS2795.1.

——, and Coauthors, 2013: Progress and challenges with Warn-on-Forecast. *Atmos. Res.*, **123**, 2–16, https://doi.org/10.1016/j.atmosres.2012.04.004.

Thompson, R. L., 2023: A comparison of right-moving supercell and quasi-linear convective system tornadoes in the contiguous United States 2003–21. *Wea. Forecasting*, **38**, 1497–1513, https://doi.org/10.1175/WAF-D-23-0006.1.

——, R. Edwards, J. A. Hart, K. L. Elmore, and P. Markowski, 2003: Close proximity soundings within supercell environments obtained from the Rapid Update Cycle. *Wea. Forecasting*, **18**, 1243–1261, https://doi.org/10.1175/1520-0434(2003)018<1243:CPSWSE>2.0.CO;2.

——, B. T. Smith, J. S. Grams, A. R. Dean, and C. Broyles, 2012: Convective modes for significant severe thunderstorms in the contiguous United States. Part II: Supercell and QLCS tornado environments. *Wea. Forecasting*, **27**, 1136–1154, https://doi.org/10.1175/WAF-D-11-00116.1.

Trapp, R. J., S. A. Tessendorf, E. S. Godfrey, and H. E. Brooks, 2005: Tornadoes from squall lines and bow echoes. Part I: Climatological distribution. *Wea. Forecasting*, **20**, 23–34, https://doi.org/10.1175/WAF-835.1.

Ungar, M. D., and M. C. Coniglio, 2023: Using radiosonde observations to assess the "three ingredients method" to forecast QLCS mesovortices. *Wea. Forecasting*, **38**, 2441–2460, https://doi.org/10.1175/WAF-D-22-0176.1.

Unidata 2019: NetCDF4 version 1.6. UCAR/NSF Unidata Program Center, https://doi.org/10.5065/D6H70CW6.

van der Walt, S., J. L. Schönberger, J. Nunez-Iglesias, F. Boulogne, J. D. Warner, N. Yager, E. Gouillart, and T. Yu, 2014: Scikit-image: Image processing in Python. *PeerJ*, **2**, e453, https://doi.org/10.7717/peerj.453.

Brought to you by NOAA Library | Unauthenticated | Downloaded 09/14/26 03:13 PM UTC

Virtanen, P., and Coauthors, 2020: SciPy 1.0: Fundamental algorithms for scientific computing in Python. *Nat. Methods*, **17**, 261–272, https://doi.org/10.1038/s41592-019-0686-2.

Weisman, M. L., and R. J. Trapp, 2003: Low-level mesovortices within squall lines and bow echoes. Part I: Overview and dependence on environmental shear. *Mon. Wea. Rev.*, **131**, 2779–2803, https://doi.org/10.1175/1520-0493(2003)131<2779:LMWSLA>2.0.CO;2.

——, and R. Rotunno, 2004: "A theory for strong long-lived squall lines" revisited. *J. Atmos. Sci.*, **61**, 361–382, https://doi.org/10.1175/1520-0469(2004)061<0361:ATFSLS>2.0.CO;2.

Wheatley, D. M., K. H. Knopfmeier, T. A. Jones, and G. J. Creager, 2015: Storm-scale data assimilation and ensemble forecasting with the NSSL experimental Warn-on-Forecast System. Part I: Radar data experiments. *Wea. Forecasting*, **30**, 1795–1817, https://doi.org/10.1175/WAF-D-15-0043.1.

Wilson, K. A., P. L. Heinselman, C. M. Kuster, D. M. Kingfield, and Z. Kang, 2017: Forecaster performance and workload: Does radar update time matter? *Wea. Forecasting*, **32**, 253–274, https://doi.org/10.1175/WAF-D-16-0157.1.

——, ——, P. S. Skinner, J. J. Choate, and K. E. Klockow-McClain, 2019: Meteorologists' interpretations of storm-scale ensemble-based forecast guidance. *Wea. Climate Soc.*, **11**, 337–354, https://doi.org/10.1175/WCAS-D-18-0084.1.

Xu, X., M. Xue, and Y. Wang, 2015: Mesovortices within the 8 May 2009 bow echo over the central United States: Analyses of the characteristics and evolution based on Doppler radar observations and a high-resolution model simulation. *Mon. Wea. Rev.*, **143**, 2266–2290, https://doi.org/10.1175/MWR-D-14-00234.1.

Yussouf, N., and K. H. Knopfmeier, 2019: Application of the Warn-on-Forecast System for flash-flood-producing heavy convective rainfall events. *Quart. J. Roy. Meteor. Soc.*, **145**, 2385–2403, https://doi.org/10.1002/qj.3568.

——, E. R. Mansell, L. J. Wicker, D. M. Wheatley, and D. J. Stensrud, 2013: The ensemble Kalman filter analyses and forecasts of the 8 May 2003 Oklahoma City tornadic supercell storm using single- and double-moment microphysics schemes. *Mon. Wea. Rev.*, **141**, 3388–3412, https://doi.org/10.1175/MWR-D-12-00237.1.

——, D. C. Dowell, L. J. Wicker, K. H. Knopfmeier, and D. M. Wheatley, 2015: Storm-scale data assimilation and ensemble forecasts for the 27 April 2011 severe weather outbreak in Alabama. *Mon. Wea. Rev.*, **143**, 3044–3066, https://doi.org/10.1175/MWR-D-14-00268.1.

——, J. S. Kain, and A. J. Clark, 2016: Short-term probabilistic forecasts of the 31 May 2013 Oklahoma tornado and flash flood event using a continuous-update-cycle storm-scale ensemble system. *Wea. Forecasting*, **31**, 957–983, https://doi.org/10.1175/WAF-D-15-0160.1.

——, T. A. Jones, and P. S. Skinner, 2020a: Probabilistic high-impact rainfall forecasts from landfalling tropical cyclones using Warn-on-Forecast System. *Quart. J. Roy. Meteor. Soc.*, **146**, 2050–2065, https://doi.org/10.1002/qj.3779.

——, K. A. Wilson, S. M. Martinaitis, H. Vergara, P. L. Heinselman, and J. J. Gourley, 2020b: The coupling of NSSL Warn-on-Forecast and FLASH systems for probabilistic flash flood prediction. *J. Hydrometeor.*, **21**, 123–141, https://doi.org/10.1175/JHM-D-19-0131.1.

Zhou, X., and Coauthors, 2022: The development of the NCEP Global Ensemble Forecast System version 12. *Wea. Forecasting*, **37**, 1069–1084, https://doi.org/10.1175/WAF-D-21-0112.1.

Brought to you by NOAA Library | Unauthenticated | Downloaded 09/14/26 03:13 PM UTC